Late Jurassic to Early Cretaceous age of the Daqiao gold deposit, West Qinling Orogen, China: Implications for regional metallogeny

Yafei Wu [1,2,3] Jianwei Li [1,3†] Katy Evans [2] Paulo M. Vasconcelos [4] David S. Thiede [4] Denis Fougerouse [2] Kirsten Rempel [2]

[1] State Key Laboratory of Geological Processes and Mineral Resources, China University of Geosciences, Wuhan 430074, China

[2] School of Earth and Planetary Sciences, The Institute for Geoscience Research (TIGeR), Curtin University, GPO Box U1987, Perth, WA 6845, Australia

[3] School of Earth Resources, China University of Geosciences, Wuhan 430074, China

[4] School of Earth Sciences, The University of Queensland, Brisbane 4072, Australia

†Corresponding author:
E-mail: jwli@cug.edu.cn
Phone: +86 27 67884925
Fax: +86 27 67885096

Abstract

The West Qinling Orogen is endowed with more than 100 sediment-hosted gold deposits with an estimated resource of >2,000 t Au. Previous radiometric dating results have shown that most deposits formed during a Late Triassic to Early Jurassic period of contractional deformation over the orogen. Here we show that the world-class Daqiao gold deposit formed in latest Jurassic to Early Cretaceous in a different tectonic regime. The recently discovered Daqiao gold deposit (>105 t at 3–4 g/t) in the southern belt of the West Qinling Orogen is hosted in weakly metamorphosed Triassic turbidites and is spatially associated with hydrothermally altered granodiorite and diorite porphyry dykes. Six granodiorite dykes have similar zircon U-Pb ages ranging from 215.0 ± 1.1 to 211.5 ± 1.5 Ma (1σ), whereas one diorite porphyry has a zircon U-Pb age of 187.5 ± 2.1 Ma (1σ). The age of gold mineralization is constrained by two types of sericite: sericite aggregates coexisting with disseminated auriferous pyrite in relatively high-grade breccia ores and sericite coexisting with auriferous pyrite in weakly mineralized granodiorite dykes. Sericite aggregates from the breccia ores have $^{40}Ar/^{39}Ar$ plateau ages of 150.7 ± 3.1 to 142.3 ± 2.5 Ma (2σ), whereas grains from the altered granodiorite dykes and low-grade breccia ore have $^{40}Ar/^{39}Ar$ plateau ages of 130.8 ± 3.1 to 127.2 ± 0.6 Ma (2σ). The $^{40}Ar/^{39}Ar$ ages thus suggest two periods of gold mineralization in the latest Jurassic and Early Jurassic that are likely associated with repeated brecciation at Daqiao. This Jurassic-Cretaceous mineralization ages coincide with discounted ages from several other gold deposits in the region and suggest that there is an underappreciated gold

event in the West Qinling Orogen that may not have been associated with the orogenic deformation but is genetically related to the far-field effects of plate reorganization during paleo-Pacific subduction beneath the eastern Eurasian continent.

Keywords Daqiao gold deposit • Sericite $^{40}Ar/^{39}Ar$ dating • Multistage gold mineralization • West Qinling Orogen • Paleo-Pacific plate

Introduction

The West Qinling Orogen (WQO) formed during the closure of the Paleo-Tethys and subsequent orogenesis in Late Triassic (Fig. 1) and is one of the largest and most prospective gold provinces in China with over 2,000 t of proven gold reserves (Mao et al. 2002; Chen et al. 2004; Zeng et al. 2012; Goldfarb et al. 2014; Liu et al. 2015). Previous $^{40}Ar/^{39}Ar$ dates and Rb/Sr isochron dates on K-bearing alteration minerals or fluid inclusions extracted from quartz and Rb/Sr isochron dates on pyrite have a large range as follows: 210 to 170 Ma (Mao et al. 2002), 220 to 100 Ma with a peak at 170 Ma (Chen et al. 2004), and 233 and 210 Ma (Dong and Santosh 2016). However, based on detailed textural characterization on several major gold deposits in the WQO (e.g., Liba, Baguamiao, Liziyuan, Huachanggou and Jianchaling; Fig. 1), recent ore-related sericite and fuchsite $^{40}Ar/^{39}Ar$, carbonate Sm-Nd, and sphalerite Rb-Sr dates cluster between ca. 216–200 Ma (e.g., Zeng et al. 2012; Liu et al. 2014; Wang et al. 2014; Hu 2015; Zhang 2016; Lin et al. 2017; Yue et al. 2017). These new ages support previous interpretations that gold mineralization in the WQO was largely related to contractional deformation associated with continental collision between the North China Craton and South China Block or to a post-collisional transtensional to extensional regime (Mao et al. 2002; Chen et al. 2004; Chen and Santosh 2014). Previous geochronological studies with detailed textural characterization also suggest that there was a much younger, Early Cretacous (144–125 Ma; $^{40}Ar/^{39}Ar$ dates on sericite and U-Pb dates on hydrothermal zircon) period of gold mineralization at the Jianchaling, Zhaishang, Yangshan, and Donggou-Jinlongshan deposits (Huang et al. 1996; Lu et al. 2006; Qi et al. 2006; Liu et al. 2015). However, a gold mineralization event during the Early Cretaceous has been largely discounted because the distribution and the tectonic driver for mineralization at that time remain poorly understood.

In this paper, we present high-quality laser incremental heating $^{40}Ar/^{39}Ar$ results on ore-related hydrothermal sericite from the Daqiao gold deposit to provide tight constraints on the age of alteration and gold mineralization. We also use zircon U-Pb dates to constrain the ages of granodioritic and dioritic dykes within and around the mine to determine their possible relationship to gold mineralization. Together with previous work, our results confirm that the Late Jurassic to Early Cretaceous gold event in the WQO was more widespread than previously thought. Lastly, we propose an updated tectonic setting for this much younger mineralization event in the WQO.

Geological setting

The Qinling orogen is part of the Central China Orogenic Belt located between the

North China Craton and the South China Block (inset of Fig. 1). The Qinling orogen is bounded by the Lingbao-Lushan-Wuyang Fault to the north and by the Mianlue-Bashan-Xiangguang Fault to the south (Fig. 1; Mattauer et al. 1985; Ames et al. 1993; Meng and Zhang 1999). This orogenic belt links the Qilian and Kunlun orogens in the west, and connects to the Dabie ultrahigh-pressure terrane in the east (Fig. 1). The Qinling orogen formed as a result of prolonged subduction of the proto-Tethyan ocean and collision between the North China Craton and Qinling micro-plate along the Shangdan suture in the middle Paleozoic. The subduction of the paleo-Tethyan ocean and subsequent collision between the Qinling terrain and the Yangtze craton along the Mianlue suture in the early Mesozoic also played an important role in its formation (Meng and Zhang 1999; Dong et al. 2011). The final closure of the paleo-Tethyan Ocean and continental collision along the Mianlue suture is characterized by a scissor-like, diachronous suturing, that propagated progressively from east to west (Zhu et al. 1998; Chen et al. 2006; Dong et al. 2011). The Qinling orogen is divided into four terranes that are separated by the Shangdan and Mianlue suture zones and several thrust faults (Fig. 1): the Southern North China Craton, North Qinling Belt, South Qinling Belt and Northern South China Block (Xu 1992; Zhang et al. 1995). The Qinling orogen is also geographically divided into the East and West Qinling Orogens (EQO and WQO; Fig. 1) that happen to coincide with the location of the Baocheng Railway (Zhang et al. 1995) that parallels the northeast-trending Chengxian-Huixian-Fengxian Fault. This regional fault separates Triassic granitoids with distinct geochemical signatures (Zeng et al. 2014).

Both the WQO and EQO are dominated by Cambrian to Triassic marine sedimentary rocks in the south that are separated by the Shangdan suture from mélanges consisting of ophiolites and metasediments of the Neoproterozoic Kuanping and early Paleozoic Erlangping Groups in the north (Dong et al. 2011). The Xiaoqinling district in the northeastern EQO is comprised mainly of metamorphic rocks of the Neoarchean Taihua Group, including amphibolite, felsic gneiss, migmatite, and widely distributed metamorphosed supracrustal rocks (Fig. 1; Li et al. 2012a). Granitoid intrusions are widespread throughout the Qinling orogen, particularly in the northern belt of the WQO (Fig. 1). These intrusions have progressively older emplacement ages from east (200–220 Ma) to west (240–250 Ma) (e.g., Sun et al. 2002; Zeng et al. 2014; Dong and Santosh 2016), a feature consistent with the scissor-like suturing and continental collision described earlier. Late Jurassic to Early Cretaceous intrusions are rare in the WQO, but occur widely in the EQO and eastern Dabie Terrane (Fig. 1). More than 100 sediment-hosted gold deposits in the WQO, including over 10 world-class deposits (cf., Goldfarb et al. 2005) hosted in Cambrian to Triassic strata with variable metamorphism (Mao et al. 2002; Chen et al. 2004). In the EQO, gold deposits are best developed in the Neoarchean to early Paleoproterozoic metamorphic rocks in the Xiaoqinling district (Mao et al. 2008, 2010; Li et al. 2012a, b), with a small number of deposits (e.g., Donggou-Jinlongshan, Qiuling, Yindonggou) in the southern marine sequences (Liu et al. 2015).

The WQO can be further subdivided into the northern and southern belts separated by the Hezuo-Lintan-Liangdang Fault (Fig. 1; Zhang et al. 2018). The northern belt is characterized by extensive exposures of Devonian flysch sequences that were subjected to low to intermediate greenschist facies metamorphism (Mattauer et al. 1985; Mao et al. 2002). The southern belt mainly comprises an east-verging belt of Triassic turbidites with a minor proportion of Cambrian to Devonian strata, with no or low-grade metamorphism. However, these strata were strongly deformed to form a series of south-verging arc-shaped, thin-skinned thrust nappe structures during the Triassic Qinling orogeny (Zhang et al. 2001; Chen and Santosh 2014).

Geology, alteration and mineralization at Daqiao

The Daqiao deposit lies to the south of the Hezuo-Lintan-Liangdang Fault, and is hosted in the turbidite sequences of the Middle Triassic Huashiguan Formation, which are in fault contact with upper Carboniferous limestone (Figs. 1, 2; Zhang et al. 2018). The Huashiguan Formation mainly consists of siltstone, siliceous, calcareous and pelitic slates, with lesser carbonaceous slates and limestone (Zhang et al. 2018). The Daqiao gold deposit is structurally localized in an inferred NE-trending anticlinoria, with a number of associated reverse faults that mostly strike northeast (Fig. 2). Several granodiorite dykes intrude the Triassic turbidites and exhibit variable degrees of hydrothermal alteration associated with subeconomic gold mineralization locally up to 2.5 ppm gold (Fig. 3a, b). The fewer diorite porphyry dykes in the deposit are less altered than the granodiorite dykes, but locally contain carbonate minerals and fine-grained pyrite (Fig. 3c, d). These observations suggest that the granodiorite and diorite porphyry dykes emplaced before the mineralization event.

More than 100 ore bodies have been delineated in the Daqiao mine, with a total proven reserve of 105 t Au averaging 3–4 g/t (Zhang et al. 2018). Gold mineralization is developed preferentially along the NE-striking reverse faults (Fig. 2). The ores are hosted in diachronous tectonic and hydraulic breccias of the Huashiguan Formation. In tectonic breccias, silicified gold ores are often at, or near, the contact between Triassic slates and underlying Carboniferous limestone (Fig. 4a, b). The competent silicified tectonic breccias were hydraulically brecciated and cemented by a chalcedony-calcite-sulfide assemblage with up to 12 g/t Au, but no associated sericite (Fig. 4c, d). Arsenian pyrite and marcasite are the predominant ore minerals in both the tectonic and hydraulic breccia ores. They are associated with minor to trace amounts of stibnite, chalcopyrite, sphalerite, galena, arsenopyrite, pyrrhotite, unnamed uranium oxides and PGE minerals. Gangue minerals consist of quartz, calcite, sericite, kaolinite, and carbonaceous material, with minor amounts of accessory apatite and rutile (Figs. 4-6). Gold mainly occurs as invisible gold in arsenian pyrite, marcasite and less abundant fine-grained arsenopyrite (Zhang et al. 2018).

Alteration types recognized include silicification, sulfidation, sericitization, and carbonatization. Based on paragenetic and textural relations, two types of sericite related to auriferous sulfides are recognized (Figs. 5, 6): 1) sericite in strongly mineralized tectonic breccia (3–4 g/t Au) and 2) sericite in intensely altered but weakly mineralized granodiorite dykes (0.2–0.4 g/t Au). In tectonic breccia ores, sericite is closely associated with silicification and sulfidation (Fig. 5a) and consists of well-crystallized aggregates 100 to 300 μm in diameter (Fig. 5b–f). These sericite aggregates are texturally intergrown with anhedral porous pyrite, which contains fine-grained inclusions of quartz and sericite (2–20 μm across; Fig. 5e-f). Mineralized granodiorite dykes are strongly sericitized, sulfidized, and are locally crosscut by quartz-sulfide veins (Figs. 3b, 6a). Sericite in these dykes is finer-grained than that in the tectonic breccia ores (Fig. 6c-f). Such fine-grained sericite occurs as veinlets (Fig. 6b) and is texturally associated with quartz selvages that mantle igneous quartz crystals (Fig. 6d), and hydrothermal euhedral pyrite, chalcopyrite, sphalerite (Fig. 6e, f).

Laser ablation ICP-MS analysis shows that both the pyrite intergrown with the sericite in the tectonic breccia ores and the pyrite hosted in the hydrothermally altered dykes contain the same Au-Ag-As-Sb-Tl element suite (Wu et al. in press). This trace element signature is also consistent with that of pyrite in the cements of hydraulic breccias. Pyrite in tectonic breccia ores contains a mean of 5.2 ppm Au and 4,568 ppm As (n = 105), whereas pyrite in the altered dykes has a mean of 1.4 ppm Au and 6,967 ppm As (n = 5; Wu et al. in press). The intimate textural relationships between auriferous pyrite and each sericite type suggests that dating of such sericite can provide meaningful constraints on the age of gold mineralization at Daqiao.

Methods

LA-ICP-MS zircon U-Pb dating

Six granodiorite dyke (samples DQ44, DQ55, DQ63, DQ123, DQ158, and DQ161) and one diorite porphyry dyke (sample DQ187) that intrude the Triassic turbidites at Daqiao with variable degrees of hydrothermal alteration and weak gold mineralization, each weighing 1 to 2 kg, were selected for zircon separation and in-situ U-Pb isotopic analysis. Zircons were handpicked under a binocular microscope after conventional heavy liquid and magnetic separation, mounted onto an epoxy resin disc, polished and gold coated. Back-scattered electron (BSE) and cathodoluminescence (CL) imaging were used to characterize the internal structure of zircons using a FEI Quanta200 environmental SEM and a MonoCL detector attached with a JEOL 8800 electron microprobe. Zircon U-Th-Pb isotopes were analyzed by LA-ICP-MS at the State Key Laboratory of Geological Processes and Mineral Resources, China University of Geosciences, Wuhan. Laser sampling was performed using a GeoLas 2005 System and an Agilent 7500a ICP-MS instrument was used to acquire ion-signal intensities. The operating conditions and data acquisition procedures follow those described in Hu et al. (2008). Off-line selection of signals and time-drift correction and quantitative calibration for trace element analyses and U-Pb dating were performed using an in-house software ICPMSDataCal (Liu et al. 2010). Correction for common Pb was made on the basis of the ^{204}Pb measured. The 91500 zircon standard was used to calibrate U/Pb isotopic discrimination and the precision and stability of the equipment during analysis (Wiedenbeck et al. 1995). Weighted mean U-Pb ages (with 95% confidence) and concordia diagrams were obtained using Isoplot/Ex_ver3 (Ludwig, 2003).

Sericite $^{40}Ar/^{39}Ar$ dating

Four samples of tectonic breccia ores (DQ70, DQ71, DQ218, and DQ220; 3–4g/t Au) and two samples of weakly mineralized granodiorite dykes (DQ55 and DQ123; 0.2–0.4g/t Au) were collected from different boreholes and underground tunnels for sericite separation and ^{40}Ar/^{39}Ar geochronology. ^{40}Ar/^{39}Ar analysis of sericite was carried out at the University of Queensland Argon Geochronology in Earth Sciences laboratory (UQ-AGES) following the methodology described in Vasconcelos et al. (2002).

Polished thin sections of each sample were studied by transmitted and reflected light microscopy to determine the mineralogy and paragenesis of sericite. After petrographic observation, suitable parts of each sample were crushed and processed using standard density separation techniques, followed by careful hand picking under a binocular microscope to isolate pure sericite grains (0.5–2 mm, >99% purity). Sericite grains were irradiated for 14 hours in the Cadmium-lined B-1 CLICIT facility, a TRIGA-type reactor, Oregon State University, USA. After a 3-month cooling period, two aliquots of each sample were analyzed using the ^{40}Ar/^{39}Ar laser incremental heating method, with a continuous-wave Ar-ion laser (532 nm) with a 2 mm wide defocused beam. The fraction of gas released was analyzed for Ar isotopes in a MAP215-50 mass spectrometer equipped with a third C-50 SAES Zr-V-Fe getter. The J-value for each Al-disk computed from 15 individual aliquots of the neutron fluence monitor, each consisting of 1–3 crystals of Fish Canyon Sanidine, is 0.003695 ± 0.000009. The raw data were processed using MassSpec software (Version 7.527) and the ages were calculated using the decay constants recommended by Steiger and Jäger (1977).

Zircon U-Pb results

The U-Pb isotope results from weakly mineralized granodiorite dykes are tabulated in Table 1 and are plotted on concordia diagrams in Figures 7 and 8. Zircons from all samples are pale to light grey, display semi-prismatic or subhedral shapes, and range from 80 to 150 μm in length with elongation ratios of 1 to 3. With the exception of a few zircons that contain subrounded cores, most grains have simple internal growth structures with delicate oscillatory zoning as shown in the CL images. These zircon grains exhibit Th/U ratios between 0.1 and 0.6 with a mean of 0.2 (n = 85; Table 1).

Thirteen zircon analyses from sample DQ44 yield concordant U-Pb ages, with a weighted mean $^{206}Pb/^{238}U$ age of 213.0 ± 1.3 Ma (MSWD = 0.31; Fig. 7a). Twelve analyses from sample DQ55 are concordant or nearly concordant and yield a weighted mean $^{206}Pb/^{238}U$ age of 214.9 ± 1.3 Ma (MSWD = 0.42; Fig. 7b). Fifteen U-Pb analyses were performed on sample DQ63, which form a coherent group with a weighted mean $^{206}Pb/^{238}U$ age of 211.5 ± 1.5 Ma (MSWD = 1.40; Fig. 7c). Fifteen analyses of DQ123 yield concordant $^{206}Pb/^{238}U$ ages with a weighted mean of 212.0 ± 1.1 Ma (MSWD=0.85; Fig. 7d). Seventeen zircon analyses from sample DQ158 yield concordant U-Pb ages with a weighted mean $^{206}Pb/^{238}U$ age of 215.0 ± 1.1 Ma (MSWD=1.10; Fig. 7e). Seventeen zircon analyses from sample DQ161 are concordant or nearly concordant and yield a weighted mean $^{206}Pb/^{238}U$ age of 213.3 ± 1.1 Ma (MSWD = 0.62; Fig. 7f). To summarize, the LA-ICP-MS zircon U-Pb dates on the six altered granodiorite dykes at Daqiao have similar ages between 215.0 ± 1.1 and 211.5 ± 1.5 Ma.

Zircons from the diorite porphyry dyke (DQ187) are white to dark grey and range in length from 50-120 μm, with elongation ratios of 1 to 4. They occur with distinct sector zoning, or as cores overgrown by irregular concentric rims. A total of eight spot analyses were obtained from this sample. Three analyses on the cores yield $^{206}Pb/^{238}U$ ages of 210.3 ± 3.7 Ma, 213.1 ± 3.0 Ma and 212.0 ± 1.9 Ma (Table. 1), with Th/U ratios ranging from 0.1 to 0.7 (mean of 0.3). The remaining five analyses, which show Th/U ratios between 0.1 and 0.3 with a mean of 0.2, define a homogeneous population of $^{206}Pb/^{238}U$ age with a mean of 187.5 ± 2.1 Ma (MSWD = 0.71; Fig. 8).

^{40}Ar/^{39}Ar results

The $^{40}Ar/^{39}Ar$ results are listed in Table 2 and the age spectra are graphically depicted in Figures 9 and 10. An age plateau is defined as a sequence of continuous steps that contain more than 50% of the total released ^{39}Ar and yield reproducible results at the 95% confidence level (2σ). If a sequence of steps contains ^{39}Ar slightly less than 50% of the total ^{39}Ar released, but yields reproducible results, or contains more than 50% of the total ^{39}Ar released, but the age values of each step are slightly beyond the 95% confidence level (2σ), it is defined as a plateau-like spectrum (Li and Vasconcelos 2002).

In this study, most sericite samples from tectonic breccia ores yield well-developed plateau or plateau-like ages (Figs. 9, 10). Two sericite aliquots from sample DQ71 yield well-defined plateau ages of 143.2 ± 2.3 Ma and 143.8 ± 1.4 Ma that are reproducible within analytical uncertainties (Fig. 9a, b). One of two aliquots from sample DQ218 has a flat age spectrum consisting of seven consecutive heating steps that account for >80% of the total ^{39}Ar released (Fig. 9c). The plateau age of this aliquot is 142.3 ± 2.5 Ma, consistent with those of the two aliquots of sample DQ71. The other aliquot from this sample yields a descending staircase spectrum that did not reach a plateau (Fig. 9d). However, the initial low-temperature heating step has an apparent age of 147.9 ± 0.9 Ma that is within the analytical uncertainty of the plateau age of the first aliquot. The next six heating steps account for 35% of the total ^{39}Ar released and yield apparent ages ranging from 118.6 to 131.2 Ma (Table 2). Both aliquots of sample DQ220 yield a descending staircase spectrum, with five continuous intermediate steps yielding a plateau or plateau-like age of 150.7 ± 3.1 Ma and 145.9 ± 2.5 Ma, respectively (Fig. 9e, f). The first sericite aliquot of sample DQ70 yields a descending age spectrum: the initial low-temperature step accounts for 60% of the total ^{39}Ar released with an apparent age of 140.1 ± 0.5 Ma, whereas the next five steps define a younger plateau-like age of 130.8 ± 3.1 Ma (Fig. 9g). The second aliquot yields a disturbed age spectrum without geologically meaningful age information (Fig. 9h).

Four sericite grains from two hand-specimens collected from the weakly mineralized dykes were dated. The two aliquots from sample DQ55 yield perfectly flat spectra consisting of all nine heating steps with 100% of the cumulative ^{39}Ar released (Fig. 10a, b). They have extremely reproducible plateau ages of 128.8 ± 0.6 Ma and 128.6 ± 0.6 Ma, respectively. Both sericite separates from sample DQ123 also yield well-defined, reproducible plateau ages of 127.2 ± 0.6 Ma and 128.0 ± 0.6 Ma (Fig. 10c, d). These plateau ages are in excellent agreement with those of sample DQ55.

It is noteworthy that several grains from the tectonic breccia ores have anomalously younger ages defined by the high-temperature steps. These steps generally account for 10–20% of the total amount of ^{39}Ar released, with ^{40}Ar/^{39}Ar apparent ages ranging from 120–45 Ma (Table 2). These apparent ages are younger than the plateau ages and have much larger uncertainties. This type of age spectra is unusual for hydrothermal micas, and the younger apparent ages defined by the high-temperature steps likely resulted from reimplantation of recoiled ^{39}Ar into tighter crystallographic sites in sericite (Vasconcelos 1999). The fine-grained nature of the sericite dated suggests that the nucleogenic ^{39}Ar produced in the edge of sericite is susceptible to recoil during neutron irradiation with the recoiled ^{39}Ar relocated into the inner and tighter crystallographic sites of the mineral.

Timing of magmatism

The zircon U-Pb ages of hydrothermally altered and weakly mineralized granodiorite and diorite porphyry dykes provide tight constraints on the age of magmatism and its temporal relation to gold mineralization. Zircons from the granodiorite and diorite porphyry dykes mostly show oscillatory zoning, or distinct sector zoning, both of which suggest a magmatic origin (Hoskin 2000; Corfu et al. 2003). This view is further supported by the Th/U ratios (0.1–0.7, Table 1) that fall in the general range of magmatic zircons (0.1–1; Belousova et al. 2002). The six granodiorite dykes have concordant U-Pb ages in the range of 215–212 Ma, whereas the irregular concentric rims on inherited zircon cores (213–210 Ma) in the diorite porphyry dyke yield a younger U-Pb age of 187.5 ± 2.1 Ma. The core has U-Pb dates consistent with those of the six granodiorite dykes but significantly older than that of the rims. This age difference indicates that the zircon core of the diorite porphyry represents inheritance from earlier magmatic rocks represented by the granodiorite dykes investigated, whereas the U-Pb age of the rims can be interpreted as the emplacement age of the diorite porphyry dyke. The U-Pb ages presented here are consistent with previous zircon U-Pb dating results for most granitoid intrusions over vast areas of the WQO, and confirm that magmatism in and surrounding the Daqiao mine occurred in a syn- to post-collisional setting (Dong et al. 2011; Dong and Santosh 2016).

Timing of gold mineralization

With the exception of two aliquots from samples DQ70 and DQ218 (Fig. 9d, h), the remaining ten sericite grains from the breccia ores and mineralized dykes yield well-defined plateau or plateau-like ages (Figs. 9, 10). In most cases, two aliquots from the same sample have reproducible plateau or plateau-like ages, as best illustrated by samples DQ71, DQ55 and DQ123 (Figs. 9a, b, 10). In addition, the ages of different samples from the same ore type are generally consistent (e.g., sample DQ71 vs. DQ218; DQ55 vs. DQ123). The age reproducibility between different aliquots of the same sample and between different samples from the same ore type suggests that the $^{40}Ar/^{39}Ar$ results are reliable and can be interpreted as the actual precipitation ages of hydrothermal sericite. The textural relationships between sericite and gold (Figs. 5, 6) indicate that these ages are representative of gold mineralization in the tectonic breccias at Daqiao.

The $^{40}Ar/^{39}Ar$ dates suggest there were two periods of gold mineralization at Daqiao. Sericite extracted from the relatively high-grade tectonic breccia ores (samples DQ71, DQ218 and DQ220) with plateau ages of 150.7 ± 3.1 to 142.3 ± 2.5 Ma are representative of the first period of gold mineralization. This relatively large age range indicates that gold mineralization may be episodic in a prolonged hydrothermal process, as partly supported by multiple brecciation observed both in the field and petrographically (Fig. 4). The plateau-like age of sample DQ70 (130.8 ± 3.1 Ma) is significantly younger than the aforementioned plateau ages, but is comparable with the $^{40}Ar/^{39}Ar$ plateaus ages of sericite from the weakly mineralized dykes (see below). The younger age is, therefore, likely due to the superimposed growth on, or neoformation of sericite in, the early stage of mineralization. Similarly, the six consecutive intermediate- to high-temperature steps of samples DQ218 and DQ70 (Fig. 9d, g) with apparent ages ranging from 112 to 132 Ma (Table 2) are also due to the second period of hydrothermal activity.

Four sericite aggregates from the hydrothermally altered and gold mineralized dykes have extremely reproducible $^{40}Ar/^{39}Ar$ plateau ages of ca. 128 Ma (Fig. 10). These ages are 15–20 million years younger than the values of the sericite from the tectonic breccia ores, and are interpreted to be representative of the second hydrothermal event. The significance of this later gold mineralizing event in forming economic gold ores, however, is currently unclear, given that most of the mineralized dykes contain no more than 0.4 g/t Au.

Collectively, the $^{40}Ar/^{39}Ar$ results suggest that the Daqiao gold deposit formed in the Latest Jurassic to Early Cretaceous, 50 million years younger than most gold deposits in the WQO (ca. 216–200 Ma; e.g., Zeng et al. 2012; Liu et al. 2014; Wang et al. 2014; Hu 2015; Zhang 2016; Lin et al. 2017; Yue et al. 2017) and the Late Triassic orogenic deformation associated with convergence between the North China Craton and South China Block (Dong et al. 2011; Dong and Santosh 2016). Gold deposits of similar ages have also been reported elsewhere in the WQO (Figs. 1, 11). For example, Lu et al. (2006) reported a well-defined $^{40}Ar/^{39}Ar$ plateau age of 125.3 ± 1.3 Ma for ore-stage sericite from the Zhaishang gold deposit in the northern belt of WQO. Similarly, hydrothermal zircon from auriferous quartz veins at the Yangshan gold deposit in the southern belt of the WQO yielded $^{206}Pb/^{238}U$ ages ranging from 137 to 121 Ma with a weighted mean of 126.9 ± 3.2 Ma (Qi et al. 2006). More recently, Liu et al. (2015) obtained a well-defined sericite $^{40}Ar/^{39}Ar$ plateau age of 142.3 ± 0.8 Ma for high-grade ores (9.3 g/t) of the Donggou-Jinlongshan gold deposit. Early Cretaceous gold mineralization is also pervasive in large areas of the EQO.

Based on molybdenite Re-Os dates and incremental $^{40}Ar/^{39}Ar$ dates on hydrothermal biotite and sericite, Li et al. (2012b) bracketed the age of seven major gold deposits in the Xiaoqinling district between 154.1 ± 1.1 Ma and 118.9 ± 1.2 Ma (n = 20). We therefore conclude that the Daqiao and other coeval gold deposits in the WQO are products of the same metallogenic event that produced gold vein deposits in EQO.

Implications for regional metallogeny

The WQO is well endowed with numerous sediment-hosted gold deposits that have been considered to be genetically related to Triassic orogenesis involving continental collision between the North China Craton and South China Block (e.g., Mao et al. 2002, 2008; Chen and Santosh 2014). Recent geochronological studies have shown that many deposits formed in a relatively restricted time interval of ca. 216–200 Ma (e.g., Zeng et al. 2012; Liu et al. 2014; Wang et al. 2014; Hu 2015; Zhang 2016; Lin et al. 2017; Fig. 11). This age interval coincides with a tectonic transition from syn-collisonal compression to post-collisional extension after the final amalgamation between the North China Craton and South China Block along the Qinling orogenic belt (Chen et al. 2004; Ye et al. 2008; Dong and Santosh 2016). This tectonic transition is associated with widespread syn-collisional granitoid intrusions (ca. 230–210 Ma; Sun et al. 2002; Gong et al. 2009; Jiang et al. 2010; Zeng et al. 2014), and post-collisional rapakivi granites (ca. 210–200 Ma) and associated mafic dykes (e.g., Qin et al. 2007, 2008, 2009). After collision, the entire Qinling orogen evolved to an intra-continental orogenic stage (Dong et al. 2011; Dong and Santosh

2016; Fig. 11).

Together with geochronologic results from several other deposits, our $^{40}Ar/^{39}Ar$ data from the Daqiao gold deposit show that there was a significant and widespread episode of gold mineralization in the Latest Jurassic to Early Cretaceous (Fig. 11). It is noteworthy that no gold deposits have formed during 185–150 Ma in the WQO (Fig. 11). The lack of gold mineralization and igneous intrusions in this time period suggests that contractional or transtensional deformation possibly ended by the Early Jurassic. The latest Jurassic to Early Cretaceous gold deposits in the WQO were likely controlled by a distinct phase of tectonism.

In the EQO (e.g., Shanzha basin, Xiaoqinling district), 150–125 Ma granitoids and polymetallic deposits, lode gold deposits, Cu-Mo porphyry-skarns, and Pb-Zn sulfide veins are widespread (Xue et al. 1996; Mao et al. 2008, 2010; Li et al. 2012a, b). Geochemical and isotopic data indicate that these granitoid intrusions were largely derived from remelting of mafic lower crust under an extensional regime coupled with asthenospheric upwelling (Xie et al. 2012, 2017; Wu et al. 2014; Yan et al. 2014).

It has been suggested that the Late Jurassic to Early Cretaceous tectonism in the EQO and the whole eastern China continent was controlled by the circum-Pacific tectonic regime (e.g., Mao et al. 2005, 2008, 2010; Sun et al. 2007). Oblique subduction of the paleo-Pacific plate beneath the Eurasian continent has been proposed to commence at ca. 160 Ma (Ren et al. 1992; Niu et al. 2003). At ca. 140 Ma, the principal stress vectors changed from NS-trending to near EW-trending (Mao et al. 2005). Subsequently, at ca. 125–122 Ma, the drifting direction of the paleo-Pacific plate changed from roughly S to NW (Koppers et al. 2003; Sun et al. 2007). We therefore tentatively link the Latest Jurassic to Early Cretaceous gold deposits in the WQO to the far-field effects of the paleo-Pacific subduction beneath the eastern Eurasian continent and the change in plate motions in the NE Asia. Recognition of a younger gold event may have contributed to the well endowment of gold mineralization in the WQO.

Conclusions

This study provides significant new insights into the age of hydrothermal alteration and gold mineralization at Daqiao. The granodiorite and diorite porphyry dykes in and around the mine formed from 215.0 ± 1.1 Ma to 187.5 ± 2.1 Ma (1σ), indicating that they are products of syn- to post-collision magmatism throughout the WQO. Sericite $^{40}Ar/^{39}Ar$ ages are much younger and suggest that there are two periods of gold mineralization: an intensely mineralized period from 150.7 ± 3.1 to 142.3 ± 2.5 Ma (2σ), followed by a less intensive period from 130.8 ± 3.1 to 127.2 ± 0.6 Ma (2σ). The geochronological data precludes a genetic relation between the magmatism and gold mineralization. We propose that Late Jurassic to Early Cretaceous gold mineralization in the WQO was related to the far-field effects of plate reorganization during paleo-Pacific subduction beneath the eastern Eurasian continent. Gold mineralization of this age appears to be widespread in the Qinling Orogen and has implications for future gold exploration in this orogenic belt.

Acknowledgments

We acknowledge the valuable support from the Daqiao Mining Ltd. and Geological Survey of Gansu Province for access to samples and information about the Daqiao deposit. Research work was financially supported by the Ministry of Science and Technology of China (2014CB440906), the National Natural Science Foundation of China (grants 41772081 and 41072057), the GPMR State Key Laboratory (MSFGPMR03), and the China Geological Survey (grant 1212011120570). The senior author acknowledges the receipt of Chinese Scholarship Council/Curtin International Postgraduate Research Scholarship. We thank Al Hofstra at the USGS in Denver and an anonymous reviewer for their constructive reviews.

References

Ames L, Tilton GR, Zhou GZ (1993) Timing of collision of the Sino-Korean and Yangtze cratons: U-Pb zircon dating of coesite-bearing eclogites. Geology 21: 339–342

Belousova EA, Griffin WL, O'Reilly SY, Fisher NL (2002) Igneous zircon: trace element composition as an indicator of source rock type. Contrib Mineral Petrol 143: 602–622

Chen YJ, Zhang J, Zhang FX, Pirajno F, Li C (2004) Carlin and Carlin-like gold deposits in western Qinling mountains and their metallogenic time, tectonic setting and model. Geol Rev 50:134–152

Chen YJ, Santosh M (2014) Triassic tectonics and mineral systems in the Qinling Orogen, central China. Geol J 49: 338–358

Chen Z, Lu S, Li H, Li H, Xiang Z, Zhou H, Song B (2006) Constraining the role of the Qinling orogen in the assembly and breakup of Rodinia: tectonic implications for Neoproterozoic granite occurrences. J Asian Earth Sci 28: 99–115

Corfu F, Hanchar JM, Hoskin PW, Kinny P (2003) Atlas of zircon textures. Rev Mineral Geochem 53: 469–500

Dong YP, Zhang GW, Neubauer F, Liu XM, Genser J, Hauzenberger C (2011) Tectonic evolution of the Qinling orogen, China: review and synthesis. J Asian Earth Sci 41:213–237

Dong YP, Santosh M (2016) Tectonic architecture and multiple orogeny of the Qinling Orogenic Belt, Central China. Gondwana Res 29: 1–40

Goldfarb RJ, Baker T, Dube B, Groves DI, Hart CJR, Gosselin P (2005) Distribution, character, and genesis of gold deposits in metamorphic terranes. Economic Geology 100th Anniversary Volume,

407–450
Goldfarb RJ, Taylor RD, Collins GS, Goryachev NA, Orlandini OF (2014) Phanerozoic continental growth and gold metallogeny of Asia. Gondwana Res 25: 48–102
Gong HJ, Zhu LM, Sun BY, Lee B, Guo B (2009) Zircon U-Pb ages and Hf isotope characteristics and their geological significance of the Shahewan, Caoping and Zhashui granitic pluton in the South Qinling orogen. Acta Petrol Sin 25: 248–264
Hoskin PW (2000) Patterns of chaos: fractal statistics and the oscillatory chemistry of zircon. Geochim Cosmochim Acta 64: 1905–1923
Hu QQ (2015) The mineralization features, mechanism and metallogenic regularity of the Fengtai Pb-Zn polymetallic ore cluster in West Qinling, China. Dissertation, Chinese Academy of Geological Sciences
Hu ZC, Gao S, Liu YS, Hu SH, Chen HH, Yuan, HL (2008) Signal enhancement in laser ablation ICP-MS by addition of nitrogen in the central channel gas. J Anal At Spectrom 23: 1093–1101
Huang WK, Gan XP, Shan ZX, Chen LX, Liu Y (1996) A study of petrology and metallognetic epoch of gold in Jianchaling deposit, Shaanxi Province. Geochem 25: 150–156
Jiang YH, Jin GD, Liao SY, Zhou Q, Zhao P (2010) Geochemical and Sr-Nd-Hf isotopic constraints on the origin of Late Triassic granitoids from the Qinling orogen, central China: implications for a continental arc to continent-continent collision. Lithos 117: 183–197
Koppers AAP, Staudigel H, Duncan RA (2003) High-resolution $^{40}Ar/^{39}Ar$ dating of the oldest oceanic basement basalts in the western Pacific basin. Geochem, Geophys, Geosyst 4: 8914
Li JW, Vasconcelos PM (2002) Cenozoic continental weathering and its implications for the palaeoclimate: evidence from $^{40}Ar/^{39}Ar$ geochronology of supergene K-Mn oxides in Mt Tabor, central Queensland, Australia. Earth Planet Sci Lett 200: 223–239
Li JW, Li ZK, Zhou MF, Chen L, Bi SJ, Deng XD, Qiu HN, Cohen B, Zhao XF (2012a) The Early Cretaceous Yangzhaiyu lode gold deposit, North China Craton: a link between craton reactivation and gold veining. Econ Geol 107: 43–79
Li JW, Bi SJ, Selby D, Chen L, Vasconcelos P, Thiede D, Zhou MF, Zhao XF, Li ZK, Qiu HN (2012b) Giant Mesozoic gold provinces related to the destruction of the North China craton. Earth Planet Sci Lett 349:26–37
Lin ZW, Zhou YZ, Qin Y, Yue SW (2017) Fuchsite $^{40}Ar/^{39}Ar$ geochronology of the Huachanggou gold Deposit and its tectonic implications. Geotectonica et Metallogenia 41: 315–327
Liu XL, Wang YT, Hu QQ, Wei R, Wang RT, Wen SW, Chen MS, Yang GH (2014) Sm-Nd isotopic dating of carbonate minerals from the Chaima gold deposit in the Fengxian-Taibai ore concentration area, Shaanxi Province and its implications. Acta Petrol Sin 30: 271–280
Liu YH, Li Z, Zhou S, Han YX, Li H, Li X, Zhou SF (2015) Geological characteristics, ore-forming ages and geological significance of Donggou-Jinlongshan gold deposit, South Qinling belt. Earth Sci Front 22: 1–13
Liu YS, Gao S, Hu ZC, Gao CG, Zong KQ, Wang DB (2010) Continental and oceanic crust recycling-induced melt-peridotite interactions in the Trans-North China Orogen: U-Pb dating, Hf isotopes and trace elements in zircons from mantle xenoliths. J Petrol 51: 537–571
Liu JJ, Dai HZ, Zhai DG, Wang JP, Wang YH, Yang LB, Mao GJ, Liu XH, Liao YF, Yu Chao, Li QZ (2015) Geological and geochemical characteristics and formation mechanisms of the Zhaishang Carlin-like type gold deposit, western Qinling Mountains, China. Ore Geol Rev 64:273–298
Ludwig KR (2003) ISOPLOT 3.00: A geochronological toolkit for Microsoft Excel: Berkeley,

California, Berkeley Geochronology Center

Lu YM, Li HG, Chen YG, Zhang GL (2006) $^{40}Ar/^{39}Ar$ dating of alteration minerals from Zhaishang gold deposit in Minxian County, Gansu Province, and its geologic significance. Miner Deposits 25: 590–597

Mao JW, Qiu YM, Goldfarb RJ, Zhang ZC, Garwin S, Fengshou R (2002) Geology, distribution, and classification of gold deposits in the western Qinling belt, central China. Miner Depos 37: 352–377

Mao JW, Xie GQ, Zhang ZH, Li XF, Wang YT, Zhang CQ, Li YF (2005) Mesozoic large-scale metallogenic pulses in North China and corresponding geodynamic settings. Acta Petrol Sin 21: 169–188

Mao JW, Xie GQ, Bierlein F, Qu WJ, Du AD, Ye HS, Pirajno F, Li HM, Guo BJ, Li YF, Yang ZQ (2008) Tectonic implications from Re-Os dating of Mesozoic molybdenum deposits in the East Qinling-Dabie orogenic belt. Geochim Cosmochim Acta 72: 4607–4626

Mao JW, Xie GQ, Pirajno F, Ye HS, Wang YB, Li YF, Xiang JF, Zhao HJ (2010) Late Jurassic-Early Cretaceous granitoid magmatism in Eastern Qinling, central-eastern China: SHRIMP zircon U-Pb ages and tectonic implications. Aust J Earth Sci 57: 51–78

Mattauer M, Matte P, Malavieille J, Tapponnier P, Maluski H, Xu Z, Lu Y, Tang Y (1985) Tectonics of the Qinling belt: build up and evolution of eastern Asia. Nature 317: 496–500

Meng QR, Zhang GW (1999) Timing of collision of the North and South China blocks: controversy and reconciliation. Geology 27: 123–126

Niu BG, He ZJ, Song B, Ren JS (2003) SHRIMP dating of the Zhangjiakou volcanic series and its significance. Geol Bull China 22: 140–141

Qi JZ, Yuan SS, Li L, Fan YX, Liu W, Gao QB, Sun B, Guo JH, Li ZH (2003) Geological and geochemical studies of Yangshan gold deposit, Gansu Province. Miner Deposits 49: 24–31

Qi JZ, Yang GC, Li L, Fan YX, Liu W (2006) Isotope geochemistry, chronology and genesis of the Yangshan gold deposit, Gansu. Geol in China 33: 1345–1353

Qin JF, Lai SC, Wang J, Li YF (2007) High-$Mg^{\#}$ adakitic tonalite from the Xichahe area, South Qinling orogenic belt (central China): petrogenesis and geological implications. Int Geol Rev 49:1145–1158

Qin JF, Lai SC, Li YF (2008) Slab break off model for the Triassic post-collisional adakitic granitoids in the Qinling Orogen, central China: zircon U-Pb ages, geochemistry, and Sr-Nd-Pb isotopic constraints. Int Geol Rev 50: 1080–1104

Qin JF, Lai SC, Diwu CR, Ju YJ, Li YF (2009) Magma mixing origin for the post-collisional adakitic monzogranite of the Triassic Yangba pluton, northwesternmargin of the South China Block: geochemistry, Sr-Nd isotopic, zircon U-Pb dating and Hf isotopic evidences. Contrib Mineral Petrol 159:389–409

Ren JS, Chen TY, Niu BG (1992) Tectonic Evolution of the Continental Lithosphere of the East China and Adjacent Area and Relevant Mineralization. Science Press, Beijing, 230p

Shao SC, Wang DB (2001) $^{39}A/^{40}Ar$ dating of three typical gold deposits and its geological significance in the Southern Qinling Region. Acta Geol Sin 75: 106–110

Steiger RH, Jäger E (1977) Subcommission on geochronology: Convention on the use of decay constants in geo- and cosmochemistry. Earth Planet Sci Lett 36: 359–362

Sun WD, Li SG, Chen YD, Li YJ (2002) Timing of synorogenic Granitoids in the South Qinling, central china: constraints on the evolution of the Qinling-Dabie orogenic belt. J Geol 110: 457–468

Sun WD, Ding X, Hu YH, Li XH (2007) The golden transformation of the Cretaceous plate subduction in the west Pacific. Earth Planet Sci Lett 262: 533–542

Vasconcelos PM (1999) K-Ar and $^{40}Ar/^{39}Ar$ geochronology of weathering processes. Ann Rev Earth Planet Sci 27: 183–229

Vasconcelos PM, Onoe AT, Kawashita K, Soares AJ, Teixeira W (2002) $^{40}Ar/^{39}Ar$ geochronology at the Instituto de Geociências, USP: instrumentation, analytical procedures, and calibration: Ann Brazil Acad Sci 74: 297–342

Wang KY (2000) The geological conditions of formation and mineralization features of micro-fine disseminated gold deposits in China. Geol Precious Met 9: 160-165

Wang YT, Li X, Wang RT, Liu XL, Hu QQ, Li JH (2014) Evidence of Ar-Ar Age for the metallogenic epoch of Simaoling gold deposit in Fengxian-Taibai ore cluster of Shaanxi. J Earth Sci Environ 36: 61–72

Wiedenbeck M, Alle P, Corfu F, Griffin WL, Meier M, Oberli F, Von Quadt A, Roddick JC, Spiegel W (1995) Three natural zircon standards for U-Th-Pb, Lu-Hf, trace element and REE analyses. Geostand Newsl 19: 1–23

Wu FF, Wang ZQ, Yan Z, Chen L, Xia CL, Guo YH, Peng YM (2014) Geochemical characteristics, zircons U-Pb ages and Lu-Hf isotopic composition of the Yanshanian intermediate-acidic plutons in the Shanyang-Zhashui areas, Qinling Orogenic Belt. Acta Petrol Sin 30: 451–471

Xie GQ, Ren T, Li JB, Wang RT, Xian CL, Gou YH, Dai JZ, Shen ZC (2012) Zircon U-Pb age and petrogenesis of ore-bearing granitoid for the Chigou Cu-Mo deposit from the Zhashan basin, Shaanxi Province. Acta Petrol Sin 28: 15–26

Xie GQ, Mao JW, Wang RT, Meng DM, Sun J, Dai JZ, Ren T, Li JB, Zhao HJ (2017) Origin of the Lengshuigou porphyry-skarn Cu deposit in the Zha-Shan district, South Qinling, central China, and implications for differences between porphyry Cu and Mo deposits. Miner Depos 52: 621–639

Xu ZQ (1992) Mountain-building process of the Songpan-Ganzi orogenic belt, China. Geological Publishing House, Beijing

Xue F, Lerch MF, Kroener A, Reischmann T (1996) Tectonic evolution of the East Qinling Mountains, China, in the Paleozoic: a review and new tectonic model. Tectonophysics 253: 271–284

Yan Z, Wang ZQ, Chen L, Liu SW, Ren T, Xu XX, Wang RT (2014) Tectono-magmatism and metallogeneses of Shanyang-Zhashui ore concentration area in Qinling Orogen. Acta Petrol Sin 30: 401–414

Ye HS, Mao JW, Li YF, Guo BJ, Zhang CQ, Liu WJ, Yan QR, Liu GY (2008) SHRIMP zircon U-Pb andmolybdenite Re-Os dating for the superlarge Donggou porphyry Mo deposit in East Qinling, China, and its geological implication. Acta Geol Sin 80: 1078–1088

Yin Y, Zhao YQ (2006) Relationship between granite and gold mineralization in the gold enrichment area of western Qinling, Gansu province. Gansu Geol 15: 36–41

Yue SW, Deng XH, Bagas L, Lin ZW, Fang J, Zhu CH, Zhang W (2017) Fluid inclusion geochemistry and 40Ar/39Ar geochronology constraints on the genesis of the Jianchaling Au deposit, China. Ore Geol Rev 80: 676–690.

Zeng QT, McCuaig TC, Hart CJR, Jourdan F, Muhling J, Bagas L (2012) Structural and geochronological studies on the Liba goldfield of the West Qinling Orogen, Central China. Miner Depos 47: 799–819

Zeng QT, Mccuaig TC, Tohver E, Bagas L, Lu YJ (2014). Episodic Triassic magmatism in the western South Qinling Orogen, central China, and its implications. Geol J 49: 402–423

Zhang GW, Zhang ZQ, Dong YP (1995) Nature of main tectono-lithostratigraphic units of the Qinling

Orogen: implications for the tectonic evolution. Acta Geol. Sin 11: 101–114
Zhang GW, Zhang BR, Yuan XC, Xiao QH (2001) Qinling orogenic belt and continental dynamics. Science Press, Beijing
Zhang J (2016) Study of mineralization process and mechanism in Baguamiao super large gold deposit, Fengtai ore region, Shaanxi, China. Dissertation, Chinese Academy of Geological Sciences
Zhang ZP, Wu YF, Li JW (2018) Characteristics and Genesis of the silicified breccias in the Daqiao gold deposit, West Qinling Orogen: Geol Sci Technol Inform 37: 79−88
Zhu RX, Yang ZY, Wu HN, Ma XH, Huang BC, Meng ZF, Fang DJ (1998) Paleomagnetic constraints on the tectonic history of the major blocks of China duing the Phanerozoic: Sci China Ser D: Earth Sciences 41: 1–19

Figure and table captions

Fig. 1 A simplified map of geotectonic terranes in the Qinling-Dabie orogenic belt (modified from Dong and Santosh 2016). Also shown is the distribution of the major faults, plutons, gold deposits, and the location of Daqiao gold mine study area (red box). The inset shows the location of the Qinling orogen in China. Abbreviations: *LLWF* = Lingbao-Lushan-Wushan Fault; *LLF* = Luonan-Luanchuan Fault; *SDS* = Shangdan Suture; *HLLF* = Hezuo-Lintan-Liangdang Fault; *ZCHF* = Zhouqu-Chengxian-Huixian Fault; *CHFF* = Chengxian-Huixian-Fengxian Fault; *MLS* = Mianlue Suture; *MBXF* = Mianlue-Bashan-Xiangguang Fault; *S-NCC* = Southern North China Craton; *NQB* = North Qinling Belt; *SQB* = South Qinling Belt; *N-SCB* = Northern South China Block; *Dabie UHP* = Dabie ultrahigh pressure; *WQO* = West Qinling Orogen; *EQO* = East Qinling Orogen.

Fig. 2 Geologic map of the Daqiao gold deposit (modified after Zhang et al. 2018).

Fig. 3 Photographs showing typical features of the granodiorite and diorite porphyry dykes at Daqiao. **a** Granodiorite dyke intruding silicified slate of the Triassic Huashiguan Formation. **b** Altered granodiorite dyke with intense sericitization and sulfidation crosscut by quartz-pyrite vein. **c** Diorite porphyry dyke of ca. 2 m thickness showing relatively weak hydrothermal alteration. **d** Diorite porphyry dyke with carbonation of feldspar phenocrysts. Abbreviations: *Cc* calcite, *Py* pyrite, *Qz* quartz, *Ser* sericite.

Fig. 4 Photographs (a–c) and photomicrograph (d) showing features of the breccia ores at Daqiao. **a** Contact between limestone of Middle and Upper Carboniferous Minhe Formation ($C_{2+3}m$) and breccia ores hosted in Middle Triassic Huashiguan Formation (T_2h). **b** Tectonic breccia ores consisting of angular fragments of slate and limestone. **c** Two stages of hydraulic fracturing. Black silicified tectonic breccias surrounded by hydrothermal chalcedony and pyrite, which were in turn cemented by a calcite-pyrite matrix. **d** Tectonic breccia fragment cemented by a calcite-pyrite matrix in the hydraulic breccia ores. Abbreviations: *Cal* chalcedony, *Cc* calcite, *Py* pyrite.

Fig. 5 Photographs (a) and photomicrographs (plane-polarized: b; transmitted: c, d; back-scattered electron (BSE): e, f) showing the features of sericite in tectonic breccia ores at Daqiao. **a** Relatively high grade ores (>4 g/t Au) with intense sericitization and sulfidation. **b-d** Sericitic alteration zone characterized by aggregates of sericite and coexisting auriferous pyrite in the breccia ores. **e-f** BSE images showing sericite intergrown with porous pyrite that contains fine-grained inclusions of quartz and sericite. Abbreviations: *Py* pyrite, *Qz* quartz, *Ser* sericite.

Fig. 6 Photographs (a) and photomicrographs (plane-polarized: b; transmitted: c, d; BSE: e, f) showing the features of sericite in altered granodiorite dykes at Daqiao. **a** Weakly mineralized granodiorite dyke with intense sericitization and sulfidation. **b** sericite-pyrite veinlets in altered granodiorite dykes. **c** Fine-grained sericite intergrown with irregular pyrite. **d** Pyrite, sericite, and narrow hydrothermal quartz selvages on igneous quartz. **e** Aggregates of fine-grained sericite intergrown with pyrite and minor chalcopyrite in the cracks of pyrite from altered granodiorite dykes. **f** sericte intergrown with pyrite, chalcopyrite and spalerite. Abbreviations: *Bt* biotite, *Ccp* chalcopyrite, *Py* pyrite, *Qz* quartz, *Ser* sericite, *Sp* sphalerite.

Fig. 7 Zircon U-Pb concordia diagrams for granodiorite dykes in and around the Daqiao gold mine.

Fig. 8 Zircon U-Pb concordia diagram for the diorite porphyry dyke from the Daqiao gold mine.

Fig. 9 $^{40}Ar/^{39}Ar$ age spectra of sericite from tectonic breccia ores in the Daqiao gold deposit.

Fig. 10 $^{40}Ar/^{39}Ar$ age spectra of sericite from weakly mineralized dykes in and around the Daqiao gold mine.

Fig. 11 A sketch illustrating the timing of tectonic events (Ren et al. 1992; Niu et al. 2003; Dong et al. 2011; Dong and Santosh 2016) and gold mineralization in the WQO (Wang 2000; Shao and Wang 2001; Qi et al. 2003, 2006; Lu et al. 2006; Yin and Zhao 2006; Zeng et al. 2012; Liu et al. 2014; Wang et al. 2014; Hu 2015; Zhang et al. 2016; Lin et al. 2017; Yue et al. 2017).

Table 1 LA-ICP-MS zircon U-Pb isotope data for granodiorite and diorite porphyry dykes from the Daqiao gold deposit in the West Qinling Orogen.

Table 2 Laser incremental heating $^{40}Ar/^{39}Ar$ data on hydrothermal sericite from the Daqiao gold deposit in the West Qinling Orogen.

Fig. 1

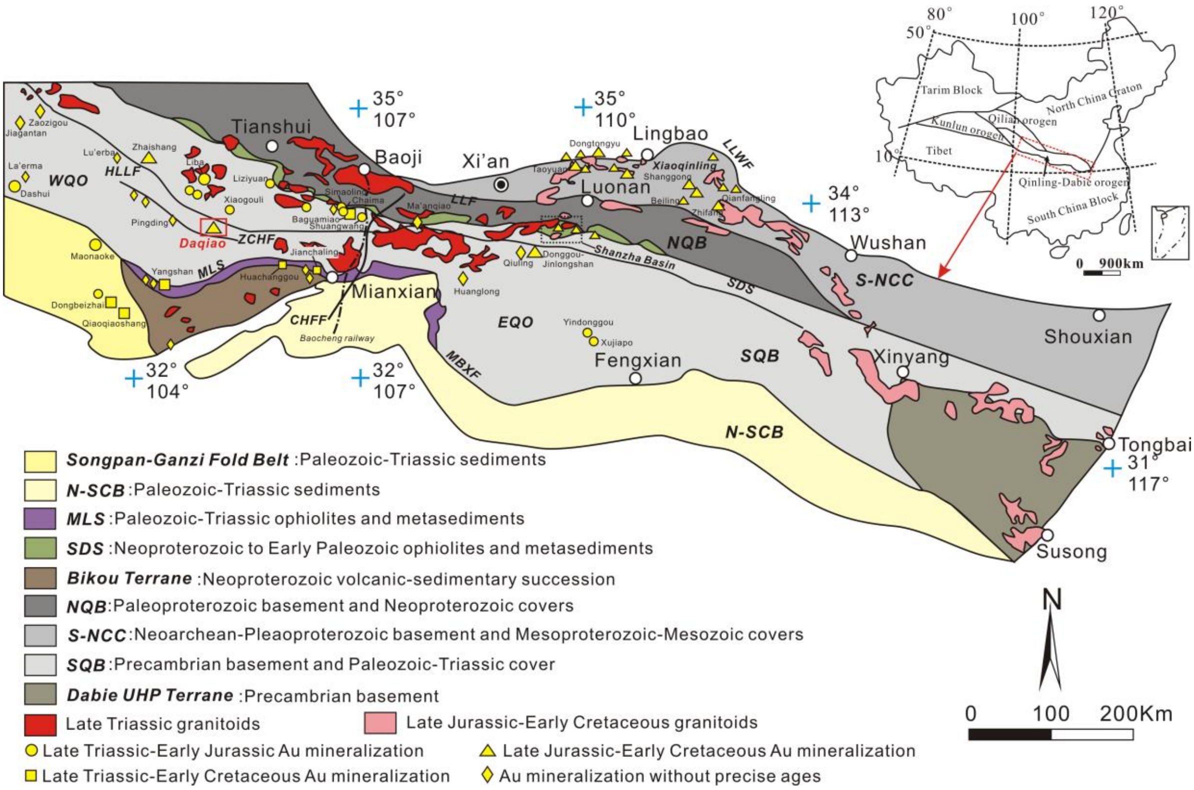
80°
100°
120°
50°
10°
Tarim Block
North China Craton
Qilian orogen
Kunlun orogen
Tibet
Qinling-Dabie orogen
South China Block
0 900km
35° 107°
35° 110°
34° 113°
32° 104°
32° 107°
31° 117°
Tianshui
Baoji
Xi'an
Lingbao
Luonan
Wushan
Mianxian
Fengxian
Xinyang
Shouxian
Tongbai
Susong
Zaozigou
Jiagantan
La'erma
Dashui
Lu'erba
Zhaishang
Liba
Liziyuan
Xiaogouli
Pingding
Daqiao
Maonaoke
Yangshan
Huachanggou
Jianchaling
Dongbeizhai
Qiaoqiaoshang
Simaoling
Chaima
Baguamiao
Shuangwang
Ma'anqiao
Dongtongyu
Taoyuan
Xiaoqinling
Shanggong
Beiling
Zhifang
Qianfanling
Qiuling
Donggou-Jinlongshan
Huanglong
Yindonggou
Xujiapo
Baocheng railway
WQO
HLLF
ZCHF
MLS
CHFF
LLF
MBXF
EQO
Shanzha Basin
NQB
SDS
S-NCC
SQB
N-SCB
LLWF
Songpan-Ganzi Fold Belt :Paleozoic-Triassic sediments
N-SCB :Paleozoic-Triassic sediments
MLS :Paleozoic-Triassic ophiolites and metasediments
SDS :Neoproterozoic to Early Paleozoic ophiolites and metasediments
Bikou Terrane :Neoproterozoic volcanic-sedimentary succession
NQB:Paleoproterozoic basement and Neoproterozoic covers
S-NCC:Neoarchean-Pleaoproterozoic basement and Mesoproterozoic-Mesozoic covers
SQB:Precambrian basement and Paleozoic-Triassic cover
Dabie UHP Terrane :Precambrian basement
Late Triassic granitoids
Late Jurassic-Early Cretaceous granitoids
Late Triassic-Early Jurassic Au mineralization
Late Jurassic-Early Cretaceous Au mineralization
Late Triassic-Early Cretaceous Au mineralization
Au mineralization without precise ages
N
0 100 200Km

Fig. 2

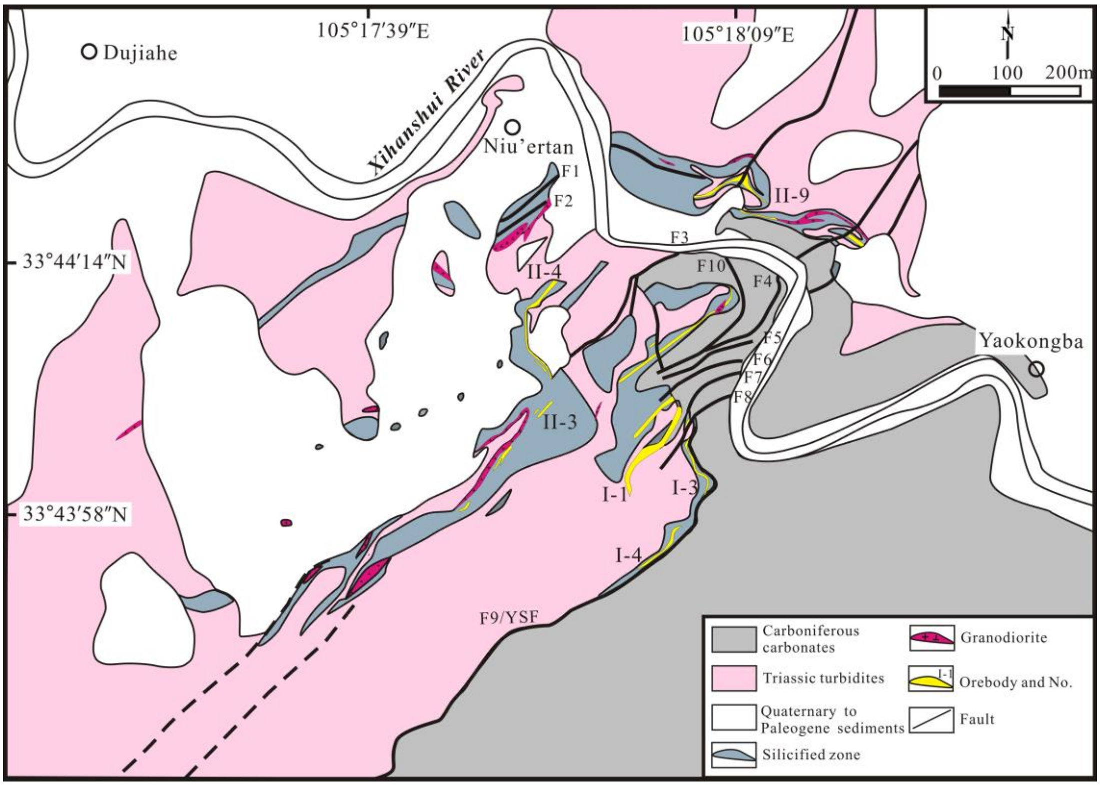
105°17'39"E
105°18'09"E
N
0 100 200m
Dujiahe
Xihanshui River
Niu'ertan
33°44'14"N
33°43'58"N
Yaokongba
F1
F2
F3
F4
F5
F6
F7
F8
F10
F9/YSF
II-9
II-4
II-3
I-1
I-3
I-4
Carboniferous carbonates
Triassic turbidites
Quaternary to Paleogene sediments
Silicified zone
Granodiorite
Orebody and No.
Fault

Fig. 3

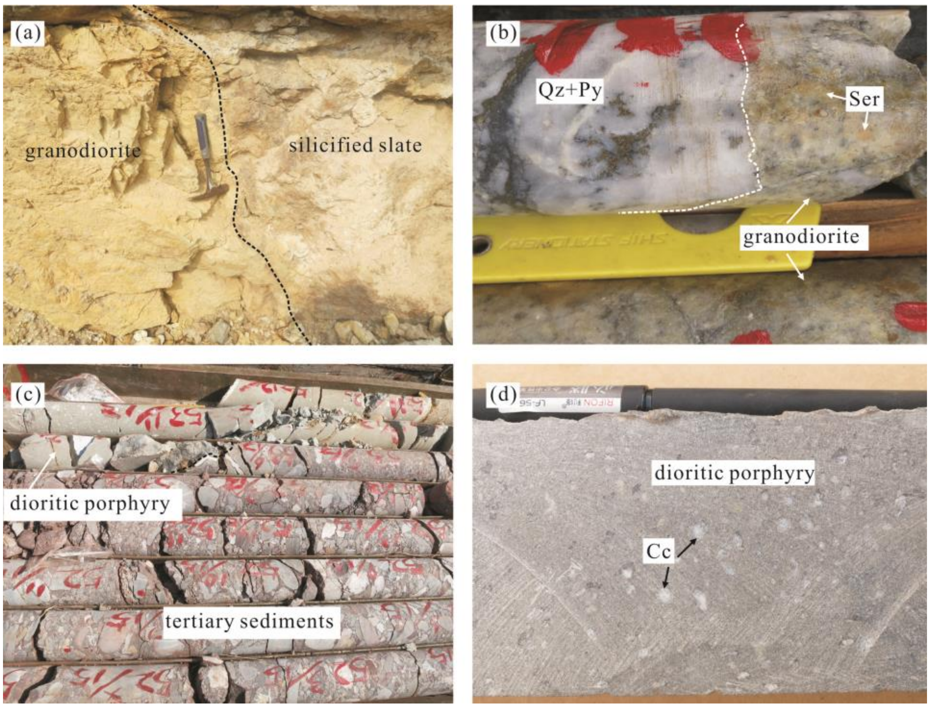
(a)
granodiorite
silicified slate
(b)
Qz+Py
Ser
granodiorite
(c)
dioritic porphyry
tertiary sediments
(d)
dioritic porphyry
Cc

Fig. 4

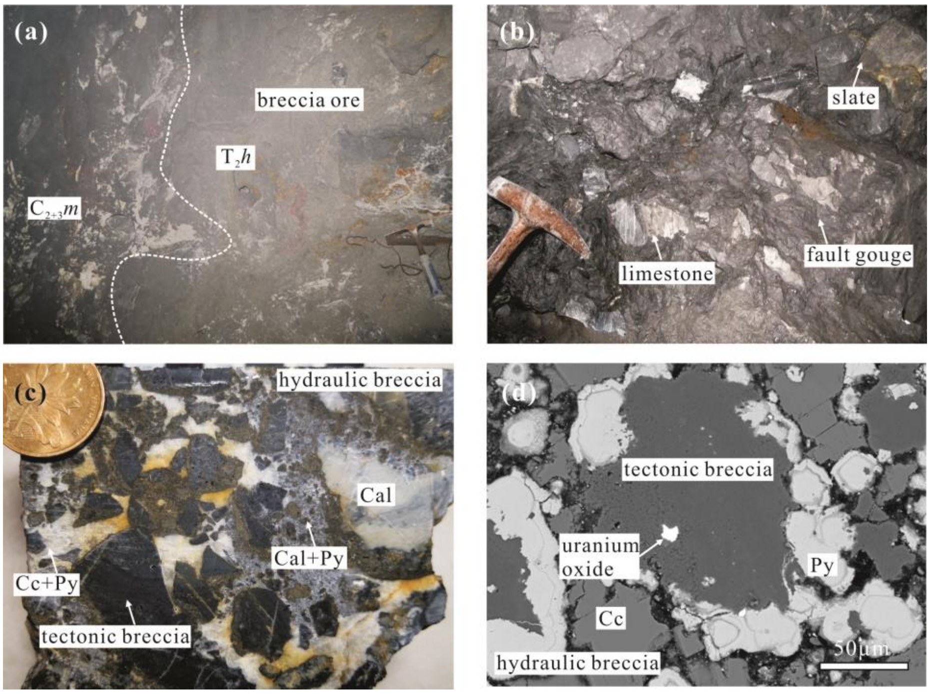
(a)
breccia ore
T_2h
$C_{2+3}m$
(b)
slate
limestone
fault gouge
(c)
hydraulic breccia
Cal
Cal+Py
Cc+Py
tectonic breccia
(d)
tectonic breccia
uranium oxide
Py
Cc
hydraulic breccia
50μm

Fig. 5

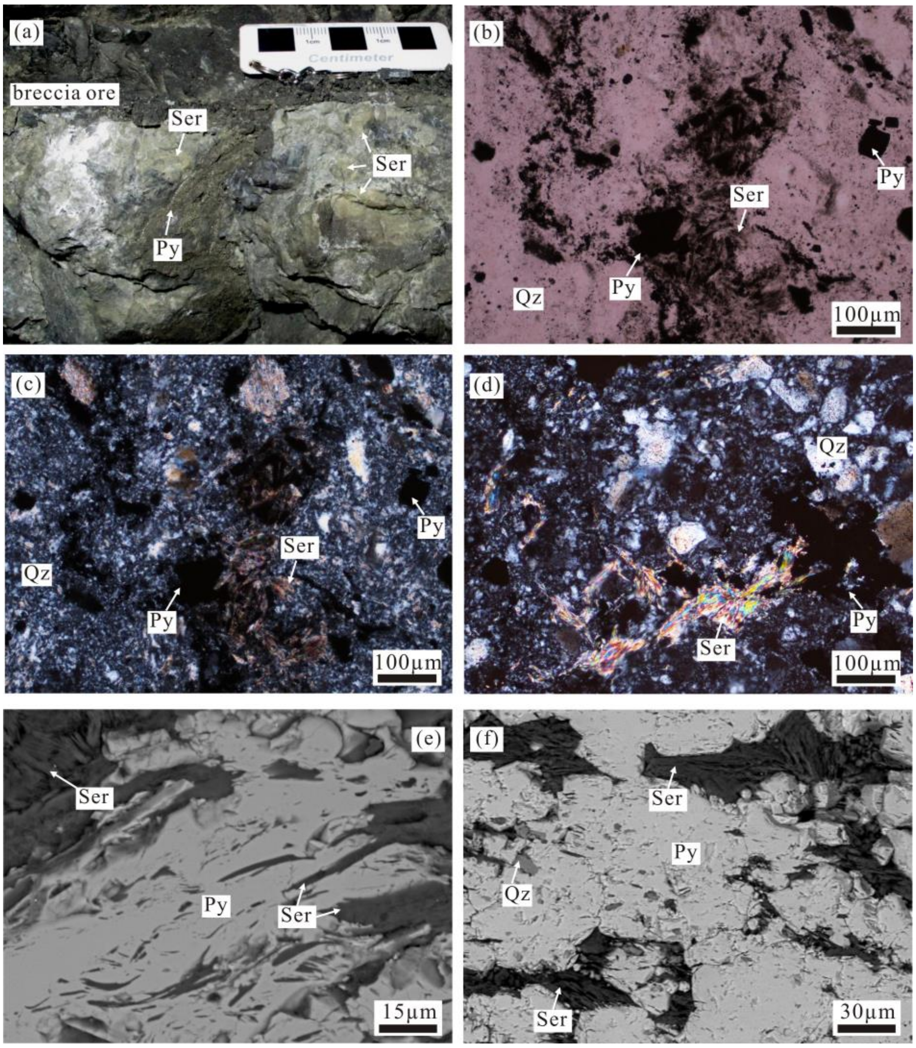
(a)
breccia ore
Ser
Ser
Py
(b)
Py
Ser
Qz
Py
100μm
(c)
Py
Ser
Qz
Py
100μm
(d)
Qz
Py
Ser
100μm
(e)
Ser
Py
Ser
15μm
(f)
Ser
Py
Qz
Ser
30μm

Fig. 6

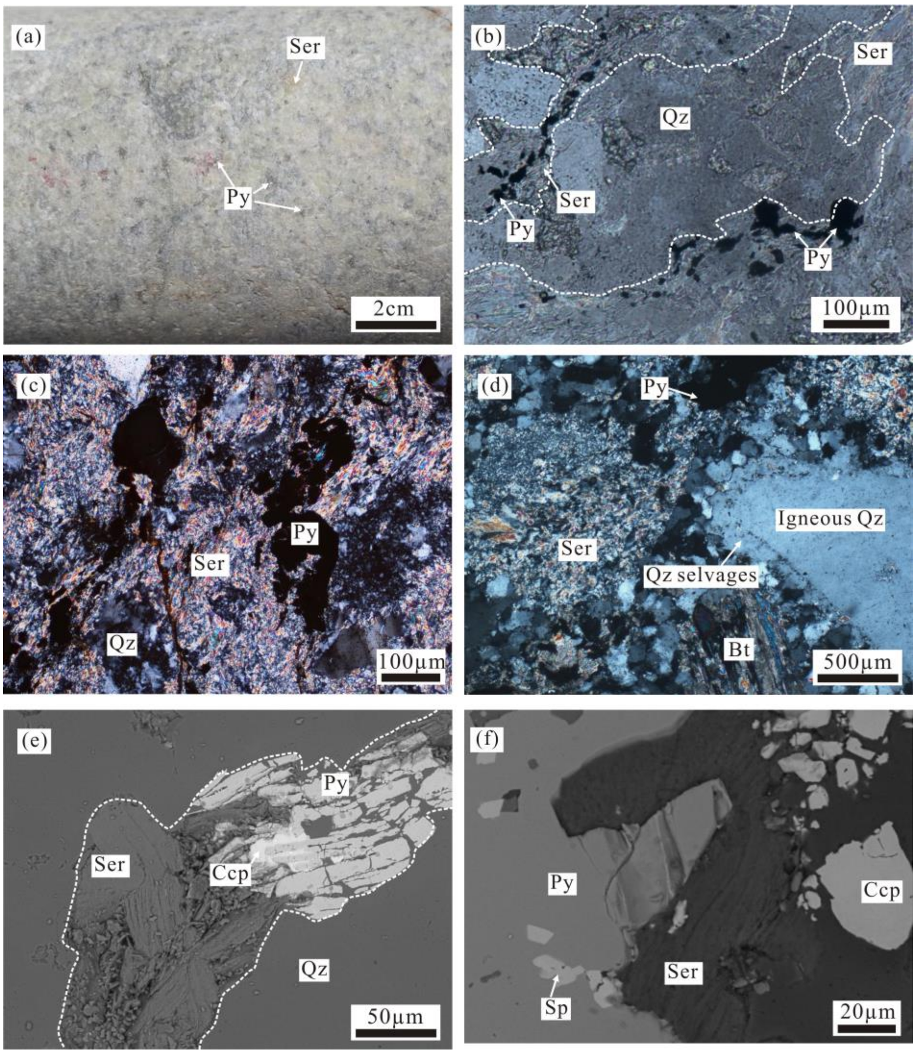

(a)
Ser
Py
2cm
(b)
Ser
Qz
Ser
Py
Py
100μm
(c)
Py
Ser
Qz
100μm
(d)
Py
Ser
Igneous Qz
Qz selvages
Bt
500μm
(e)
Py
Ser
Ccp
Qz
50μm
(f)
Py
Ccp
Ser
Sp
20μm

Fig. 7

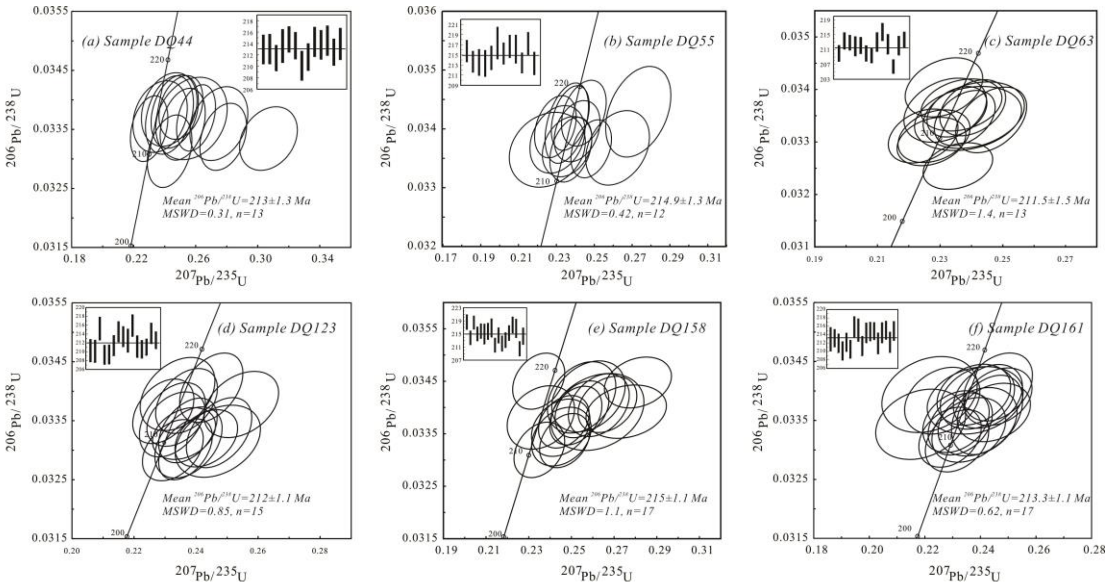
(a) Sample DQ44
Mean $^{206}Pb/^{238}U$=213±1.3 Ma
MSWD=0.31, n=13
(b) Sample DQ55
Mean $^{206}Pb/^{238}U$=214.9±1.3 Ma
MSWD=0.42, n=12
(c) Sample DQ63
Mean $^{206}Pb/^{238}U$=211.5±1.5 Ma
MSWD=1.4, n=13
(d) Sample DQ123
Mean $^{206}Pb/^{238}U$=212±1.1 Ma
MSWD=0.85, n=15
(e) Sample DQ158
Mean $^{206}Pb/^{238}U$=215±1.1 Ma
MSWD=1.1, n=17
(f) Sample DQ161
Mean $^{206}Pb/^{238}U$=213.3±1.1 Ma
MSWD=0.62, n=17
$^{206}Pb/^{238}U$
$^{207}Pb/^{235}U$

Fig. 8

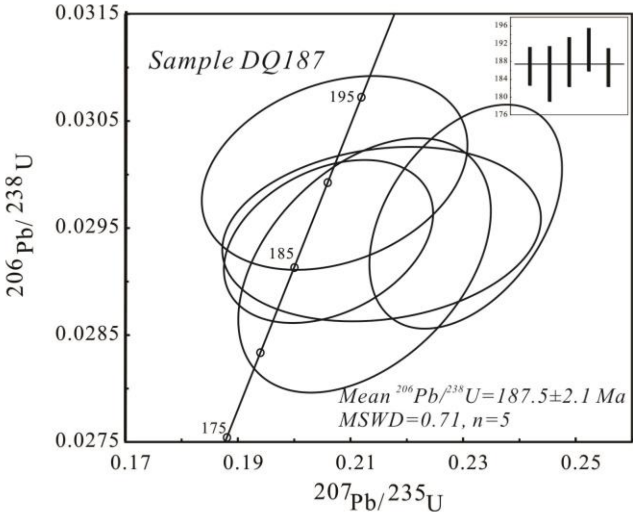
Sample DQ187
195
185
175
Mean $^{206}Pb/^{238}U$=187.5±2.1 Ma
MSWD=0.71, n=5
$^{206}Pb/^{238}U$
$^{207}Pb/^{235}U$
0.0315
0.0305
0.0295
0.0285
0.0275
0.17
0.19
0.21
0.23
0.25

739 **Fig. 9**

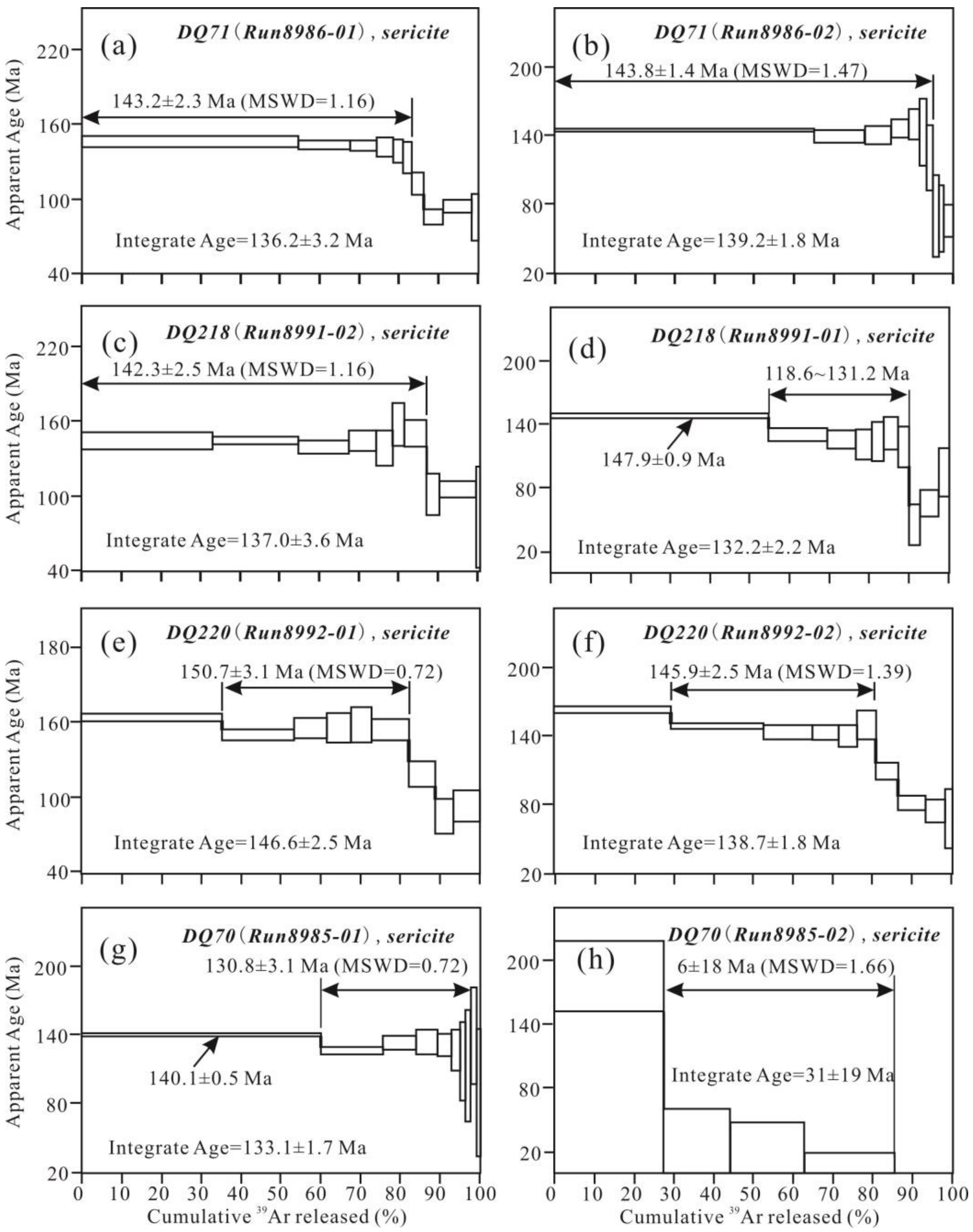

740

741

742

Fig. 10

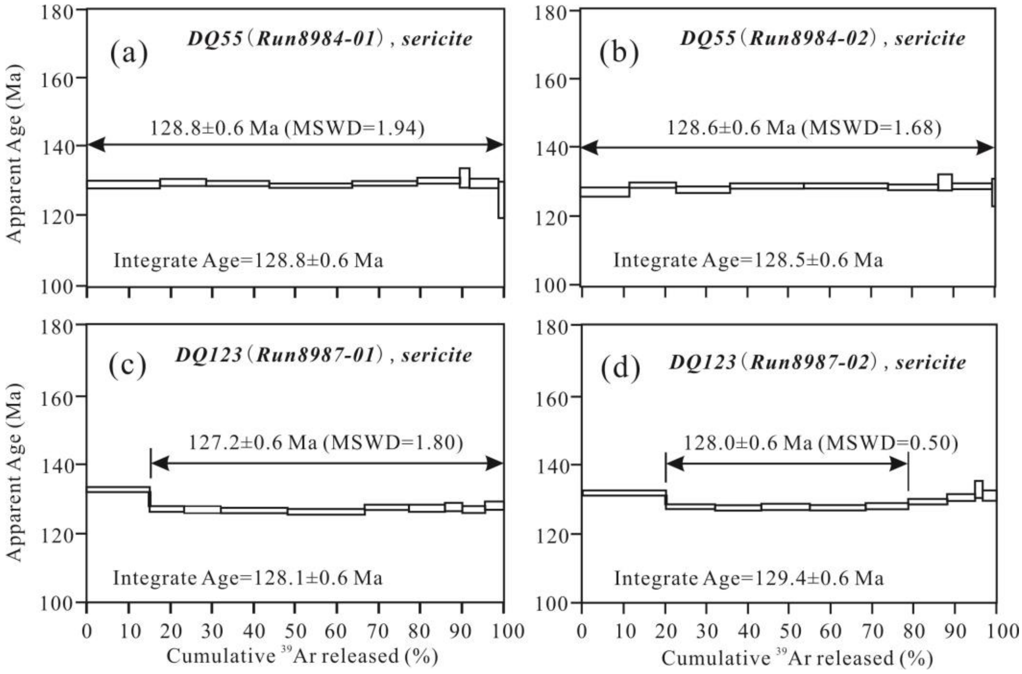
(a) DQ55 (Run8984-01), sericite
128.8±0.6 Ma (MSWD=1.94)
Integrate Age=128.8±0.6 Ma
(b) DQ55 (Run8984-02), sericite
128.6±0.6 Ma (MSWD=1.68)
Integrate Age=128.5±0.6 Ma
(c) DQ123 (Run8987-01), sericite
127.2±0.6 Ma (MSWD=1.80)
Integrate Age=128.1±0.6 Ma
(d) DQ123 (Run8987-02), sericite
128.0±0.6 Ma (MSWD=0.50)
Integrate Age=129.4±0.6 Ma
Apparent Age (Ma)
Cumulative 39Ar released (%)

Fig. 11

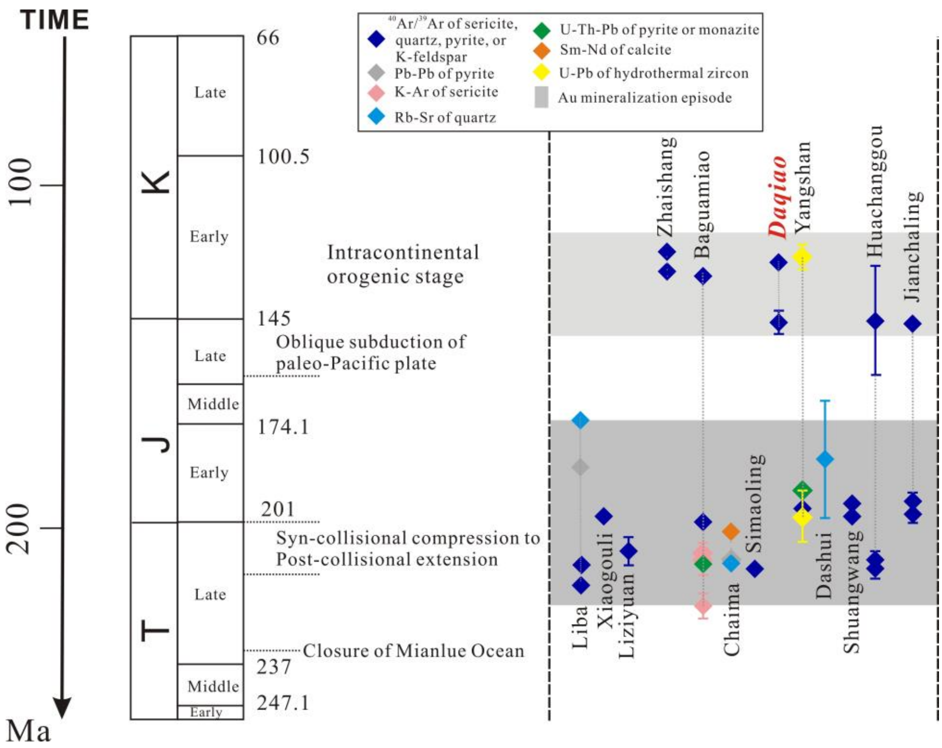
TIME
Ma
100
200
K
J
T
Late
Early
Middle
66
100.5
145
174.1
201
237
247.1
Intracontinental orogenic stage
Oblique subduction of paleo-Pacific plate
Syn-collisional compression to Post-collisional extension
Closure of Mianlue Ocean
40Ar/39Ar of sericite, quartz, pyrite, or K-feldspar
Pb-Pb of pyrite
K-Ar of sericite
Rb-Sr of quartz
U-Th-Pb of pyrite or monazite
Sm-Nd of calcite
U-Pb of hydrothermal zircon
Au mineralization episode
Liba
Xiaogouli
Liziyuan
Zhaishang
Baguamiao
Chaima
Simaoling
Daqiao
Yangshan
Dashui
Shuangwang
Huachanggou
Jianchaling

Table 1

Table 1 LA-ICP-MS zircon U-Pb isotope data of granodiorite and diorite porphyry dykes from Daqiao gold deposit in the West Qinling Orogen

		Isotope ratio						Age (Ma)					
Spot	Th/U	207Pb/206Pb	±1σ	207Pb/235U	±1σ	206Pb/238U	±1σ	207Pb/206Pb	±1σ	207Pb/235U	±1σ	206Pb/238U	±1σ
Sample DQ44													
DQ44-1	0.14	0.05	0.00	0.25	0.01	0.03	0.00	398.20	88.88	227.92	7.78	212.96	2.51
DQ44-3	0.13	0.06	0.00	0.27	0.01	0.03	0.00	572.26	93.35	246.64	9.81	213.03	2.58
DQ44-9	0.15	0.07	0.00	0.31	0.01	0.03	0.00	827.78	83.33	271.78	9.57	211.45	2.22
DQ44-10	0.19	0.06	0.00	0.26	0.02	0.03	0.00	438.94	137.02	232.47	12.28	213.57	2.88
DQ44-11	0.23	0.05	0.00	0.25	0.01	0.03	0.00	346.35	83.33	226.98	7.58	214.74	2.22
DQ44-12	0.16	0.06	0.00	0.26	0.01	0.03	0.00	453.75	74.07	234.83	6.68	213.63	2.32
DQ44-13	0.24	0.05	0.00	0.24	0.01	0.03	0.00	331.54	88.88	221.02	7.77	210.11	2.53
DQ44-14	0.16	0.06	0.00	0.28	0.01	0.03	0.00	598.17	75.91	248.88	7.91	211.63	2.34
DQ44-16	0.14	0.05	0.00	0.25	0.01	0.03	0.00	320.43	89.81	223.73	8.22	214.30	2.56
DQ44-17	0.17	0.05	0.00	0.24	0.01	0.03	0.00	227.85	111.10	216.02	9.50	213.77	2.50
DQ44-18	0.16	0.05	0.00	0.24	0.01	0.03	0.00	298.21	110.17	220.83	9.67	214.52	2.57
DQ44-19	0.19	0.05	0.00	0.23	0.01	0.03	0.00	164.90	79.62	210.18	6.59	212.50	2.30
DQ44-20	0.17	0.05	0.00	0.24	0.01	0.03	0.00	305.62	127.76	220.97	8.34	213.94	2.74
Sample DQ55													
DQ55-1	0.13	0.05	0.00	0.23	0.01	0.03	0.00	131.57	75.92	209.75	6.01	215.76	2.18
DQ55-4	0.15	0.05	0.00	0.24	0.01	0.03	0.00	233.40	54.62	214.87	7.09	213.65	2.11
DQ55-5	0.12	0.06	0.00	0.26	0.01	0.03	0.00	487.08	98.14	236.56	8.95	213.52	2.61
DQ55-6	0.13	0.05	0.00	0.23	0.01	0.03	0.00	166.75	144.43	206.25	11.01	213.32	2.62
DQ55-7	0.12	0.05	0.00	0.23	0.01	0.03	0.00	168.60	93.51	210.65	7.92	214.42	2.37
DQ55-8	0.20	0.06	0.00	0.27	0.01	0.03	0.00	527.82	87.02	245.31	9.08	217.35	3.17

DQ55-9	0.16	0.05	0.00	0.24	0.01	0.03	0.00	255.62	72.21	219.18	6.56	215.29	2.14
DQ55-12	0.34	0.05	0.00	0.24	0.01	0.03	0.00	213.04	66.66	216.25	5.45	216.68	2.27
DQ55-13	0.18	0.05	0.00	0.24	0.01	0.03	0.00	211.19	72.21	214.72	6.23	216.15	2.81
DQ55-14	0.28	0.05	0.00	0.25	0.01	0.03	0.00	346.35	62.96	225.26	5.76	213.42	2.03
DQ55-15	0.15	0.05	0.00	0.24	0.01	0.03	0.00	275.99	69.44	222.12	6.37	217.20	2.31
DQ55-16	0.36	0.05	0.00	0.24	0.01	0.03	0.00	250.07	72.21	216.48	6.01	213.33	2.27
Sample DQ63													
DQ63-1	0.15	0.05	0.00	0.22	0.01	0.03	0.00	200.08	74.06	205.71	6.08	210.00	2.12
DQ63-2	0.10	0.05	0.00	0.24	0.01	0.03	0.00	300.06	66.66	216.42	5.36	209.32	2.22
DQ63-4	0.10	0.05	0.00	0.23	0.01	0.03	0.00	250.07	61.10	212.87	5.15	207.89	2.02
DQ63-5	0.21	0.05	0.00	0.24	0.01	0.03	0.00	350.06	70.37	218.08	5.81	205.89	2.48
DQ63-6	0.14	0.06	0.00	0.28	0.01	0.03	0.00	616.69	83.32	246.88	8.87	206.98	2.08
DQ63-7	0.32	0.05	0.00	0.24	0.01	0.03	0.00	333.39	61.10	216.01	5.17	209.99	2.23
DQ63-8	0.24	0.05	0.00	0.22	0.01	0.03	0.00	172.31	74.99	204.48	6.15	206.22	1.96
DQ63-9	0.16	0.05	0.00	0.22	0.01	0.03	0.00	164.90	75.91	204.14	6.05	206.22	1.75
DQ63-10	0.13	0.05	0.00	0.23	0.01	0.03	0.00	242.66	90.73	207.83	7.22	204.75	2.37
DQ63-12	0.16	0.06	0.00	0.27	0.02	0.03	0.00	631.50	136.09	241.80	12.09	207.72	2.82
DQ63-16	0.17	0.05	0.00	0.24	0.01	0.03	0.00	294.51	65.74	215.27	6.02	207.12	1.83
DQ63-18	0.33	0.05	0.00	0.25	0.01	0.03	0.00	346.35	110.18	222.97	9.11	212.71	2.46
Sample DQ123													
DQ123-3	0.18	0.05	0.00	0.25	0.01	0.03	0.00	361.17	79.62	224.24	7.39	210.26	2.52
DQ123-5	0.14	0.05	0.00	0.24	0.01	0.03	0.00	300.06	74.99	216.54	5.87	210.12	2.50
DQ123-6	0.12	0.05	0.00	0.23	0.01	0.03	0.00	198.23	76.84	213.64	6.54	215.27	2.57
DQ123-8	0.24	0.05	0.00	0.23	0.01	0.03	0.00	231.55	62.95	212.37	5.33	209.30	2.15
DQ123-9	0.20	0.05	0.00	0.24	0.01	0.03	0.00	283.40	52.77	215.74	4.68	209.39	2.14
DQ123-10	0.26	0.05	0.00	0.24	0.01	0.03	0.00	333.39	62.96	216.37	5.09	211.40	2.27

DQ123-11	0.20	0.05	0.00	0.24	0.01	0.03	0.00	227.85	66.66	215.99	5.40	214.54	2.28
DQ123-13	0.17	0.05	0.00	0.23	0.01	0.03	0.00	166.75	60.18	209.83	5.39	213.45	2.26
DQ123-14	0.17	0.05	0.00	0.23	0.01	0.03	0.00	190.82	66.66	212.28	5.82	212.53	2.61
DQ123-15	0.15	0.05	0.00	0.25	0.01	0.03	0.00	287.10	58.33	222.51	5.49	215.94	2.44
DQ123-16	0.31	0.05	0.00	0.25	0.01	0.03	0.00	368.57	64.81	224.55	5.66	211.17	2.45
DQ123-17	0.50	0.05	0.00	0.24	0.01	0.03	0.00	327.84	62.96	221.17	5.44	210.57	2.00
DQ123-18	0.21	0.05	0.00	0.24	0.01	0.03	0.00	255.62	58.32	215.34	5.48	211.07	1.82
DQ123-19	0.15	0.05	0.00	0.25	0.01	0.03	0.00	398.20	68.51	230.39	6.43	214.17	2.32
DQ123-21	0.14	0.05	0.00	0.23	0.01	0.03	0.00	220.44	56.47	213.19	5.08	212.61	1.91
Sample DQ158													
DQ158-1	0.22	0.05	0.00	0.24	0.01	0.03	0.00	188.97	79.62	216.72	6.66	220.82	2.20
DQ158-2	0.18	0.05	0.00	0.25	0.01	0.03	0.00	338.95	36.11	229.22	6.36	218.15	2.07
DQ158-3	0.18	0.06	0.00	0.27	0.01	0.04	0.00	453.75	74.07	243.20	6.99	222.31	2.09
DQ158-4	0.32	0.05	0.00	0.26	0.01	0.03	0.00	350.06	87.03	234.01	8.16	221.55	2.22
DQ158-5	0.10	0.06	0.00	0.27	0.01	0.03	0.00	433.38	74.07	239.67	7.15	220.68	2.32
DQ158-6	0.17	0.05	0.00	0.26	0.01	0.03	0.00	383.39	103.69	234.22	9.52	219.60	2.72
DQ158-8	0.15	0.05	0.00	0.26	0.01	0.03	0.00	388.94	85.18	236.33	7.86	220.31	2.49
DQ158-9	0.15	0.05	0.00	0.26	0.01	0.03	0.00	344.50	101.84	232.14	9.24	220.28	2.82
DQ158-11	0.31	0.05	0.00	0.26	0.01	0.03	0.00	342.65	41.66	230.99	6.57	218.06	2.08
DQ158-12	0.22	0.05	0.00	0.25	0.01	0.03	0.00	305.62	80.55	227.09	6.60	217.72	2.37
DQ158-13	0.26	0.05	0.00	0.25	0.01	0.03	0.00	344.50	88.88	229.67	8.06	217.03	2.43
DQ158-14	0.17	0.05	0.00	0.25	0.01	0.03	0.00	294.51	86.10	225.87	7.66	218.18	2.25
DQ158-15	0.17	0.05	0.00	0.24	0.01	0.04	0.00	198.23	81.47	221.62	6.66	221.95	2.36
DQ158-18	0.15	0.05	0.00	0.25	0.01	0.04	0.00	198.23	92.58	223.75	7.74	225.62	2.68
DQ158-20	0.24	0.05	0.00	0.24	0.01	0.03	0.00	198.23	77.77	217.51	6.60	217.77	2.33
DQ158-21	0.15	0.05	0.00	0.23	0.01	0.03	0.00	172.31	111.10	212.54	8.73	216.99	2.61

Sample DQ161													
DQ161-1	0.16	0.05	0.00	0.24	0.01	0.03	0.00	298.21	79.62	220.58	6.89	212.95	2.79
DQ161-2	0.18	0.05	0.00	0.25	0.01	0.03	0.00	316.73	83.33	222.61	7.08	213.20	2.05
DQ161-5	0.28	0.05	0.00	0.23	0.01	0.03	0.00	213.04	49.99	212.61	6.29	212.00	2.18
DQ161-6	0.28	0.05	0.00	0.23	0.01	0.03	0.00	209.33	41.66	211.73	6.22	210.18	2.18
DQ161-7	0.17	0.05	0.00	0.23	0.01	0.03	0.00	198.23	76.84	211.40	6.50	212.23	2.17
DQ161-8	0.27	0.05	0.00	0.23	0.01	0.03	0.00	187.12	75.91	209.60	6.11	210.58	2.11
DQ161-10	0.37	0.05	0.00	0.25	0.01	0.03	0.00	305.62	80.55	223.80	6.66	215.93	2.39
DQ161-12	0.22	0.05	0.00	0.22	0.01	0.03	0.00	105.65	127.76	203.50	9.41	215.13	2.66
DQ161-13	0.42	0.05	0.00	0.24	0.01	0.03	0.00	333.39	82.40	215.19	7.19	211.35	2.27
DQ161-15	0.33	0.05	0.00	0.23	0.01	0.03	0.00	200.08	97.21	207.30	7.37	214.46	2.35
DQ161-16	0.23	0.05	0.00	0.24	0.01	0.03	0.00	257.47	85.17	217.75	7.23	214.77	2.20
DQ161-17	0.22	0.05	0.00	0.25	0.01	0.03	0.00	320.43	75.92	223.84	6.57	214.88	2.03
DQ161-18	0.21	0.05	0.00	0.22	0.01	0.03	0.00	87.13	124.06	200.84	8.90	211.95	2.47
DQ161-19	0.21	0.05	0.00	0.24	0.01	0.03	0.00	231.55	108.32	217.08	9.34	214.50	2.38
DQ161-20	0.42	0.05	0.00	0.24	0.01	0.03	0.00	211.19	82.40	216.69	7.19	215.09	2.14
DQ161-21	0.58	0.05	0.00	0.24	0.01	0.03	0.00	264.88	99.06	217.78	7.70	212.23	2.41
DQ161-22	0.34	0.05	0.00	0.24	0.01	0.03	0.00	242.66	79.62	220.82	6.67	214.92	2.24
Sample DQ187													
DQ187-02	0.73	0.06	0.00	0.24	0.02	0.03	0.00	457.45	166.65	220.31	13.75	210.29	3.74
DQ187-05	0.10	0.05	0.00	0.24	0.01	0.03	0.00	294.51	61.11	220.64	5.98	213.14	3.04
DQ187-06	0.32	0.05	0.00	0.22	0.01	0.03	0.00	346.35	122.21	197.93	9.80	186.94	2.12
DQ187-07	0.15	0.05	0.00	0.23	0.01	0.03	0.00	190.82	94.43	210.39	7.56	212.03	1.98
DQ187-08	0.26	0.05	0.00	0.21	0.01	0.03	0.00	301.91	88.88	195.40	7.70	185.11	3.03
DQ187-09	0.06	0.06	0.00	0.23	0.01	0.03	0.00	461.16	62.96	210.28	5.87	187.97	2.68
DQ187-10	0.19	0.05	0.00	0.21	0.01	0.03	0.00	190.82	109.25	191.19	8.18	190.68	2.35

DQ187-13	0.25	0.05	0.00	0.21	0.01	0.03	0.00	257.47	88.88	190.08	6.22	186.46	1.97

Table 2

Table 2 Laser incremental heating $^{40}Ar/^{39}Ar$ data on hydrothermal sericite from the Daqiao gold deposit in the West Qinling Orogen

Run ID	$^{40}Ar/^{39}Ar$	$^{37}Ar/^{39}Ar$	$^{36}Ar/^{39}Ar$	$40Ar^*/39Ar_K$	40Ar* (%)	Apparent age (Ma)	± 1 σ (Ma)	J
Sample DQ71								
8986-01A	31.247	0.023	0.02777	22.957	73.47	146.0	2.0	0.003672
8986-01B	23.412	0.256	0.00327	22.458	95.91	143.0	1.8	0.003672
8986-01C	23.410	0.306	0.00323	22.473	95.98	143.1	2.3	0.003672
8986-01D	23.120	-0.475	0.00277	22.246	96.26	141.7	3.7	0.003672
8986-01E	22.731	0.098	0.00340	21.724	95.56	138.5	4.6	0.003672
8986-01F	22.381	-0.644	0.00493	20.849	93.20	133.1	6.4	0.003672
8986-01G	20.002	0.137	0.00842	17.501	87.49	112.4	4.4	0.003672
8986-01H	24.104	0.077	0.03673	13.144	54.53	85.0	3.2	0.003672
8986-01I	25.476	-0.385	0.03649	14.547	57.12	93.9	2.4	0.003672
8986-01J	25.876	-0.227	0.04261	13.134	50.77	85.0	9.3	0.003672
8986-02A	22.909	0.009	0.00088	22.647	98.86	144.1	0.6	0.003672
8986-02B	21.370	0.808	#######	21.745	101.70	138.6	2.7	0.003672
8986-02C	22.393	0.160	0.00174	21.886	97.73	139.5	4.1	0.003672
8986-02D	22.022	-0.369	#######	22.811	103.61	145.1	4.0	0.003672
8986-02E	22.921	1.088	#######	23.437	102.18	148.9	6.6	0.003672

8986-02F	20.461	-1.496	#######	22.334	109.27	142.2	14.6	0.003672
8986-02G	16.361	-0.984	#######	18.684	114.28	119.7	14.3	0.003672
8986-02H	11.291	-1.789	0.00209	10.516	93.25	68.4	17.8	0.003672
8986-02I	20.180	0.072	0.03339	10.215	50.62	66.4	14.7	0.003672
8986-02J	17.392	0.674	0.02495	9.999	57.47	65.1	7.1	0.003672
Sample DQ218								
8991-01A	24.520	-0.131	0.00490	23.044	93.99	147.9	0.9	0.003708
8991-01B	20.185	-0.348	0.00128	19.770	97.97	127.6	2.0	0.003708
8991-01C	20.172	0.432	0.00271	19.401	96.15	125.3	4.3	0.003708
8991-01D	20.369	-0.244	0.00565	18.661	91.63	120.7	7.1	0.003708
8991-01E	21.146	0.733	0.00681	19.178	90.65	123.9	9.1	0.003708
8991-01F	21.396	1.091	0.00386	20.341	95.00	131.2	7.8	0.003708
8991-01G	20.934	2.116	0.00937	18.324	87.41	118.6	9.4	0.003708
8991-01H	18.860	0.655	0.04054	6.810	36.09	45.0	9.4	0.003708
8991-01I	24.132	0.089	0.04774	9.885	40.96	64.9	6.4	0.003708
8991-01J	25.709	0.444	0.03741	14.579	56.69	95.0	11.4	0.003708
8991-02A	41.394	-0.320	0.06407	22.235	53.73	142.9	3.4	0.003708
8991-02B	22.462	-0.047	0.00073	22.238	99.01	142.9	1.4	0.003708
8991-02C	21.999	-0.442	0.00204	21.349	97.08	137.4	2.6	0.003708
8991-02D	23.278	-1.114	0.00333	22.180	95.36	142.6	4.0	0.003708
8991-02E	24.491	0.492	0.01068	21.346	87.13	137.4	7.1	0.003708
8991-02F	25.564	-1.354	0.00383	24.294	95.12	155.6	8.5	0.003708
8991-02G	23.483	-0.159	0.00101	23.165	98.66	148.7	5.3	0.003708
8991-02H	28.069	-5.375	0.04085	15.402	55.08	100.2	8.2	0.003708
8991-02I	31.297	0.041	0.05122	16.009	51.15	104.0	3.2	0.003708
8991-02J	45.817	-8.971	0.11395	11.037	24.24	72.4	24.7	0.003708

Sample DQ220								
8992-01A	28.190	0.308	0.00982	25.288	89.69	161.7	1.4	0.003708
8992-01B	23.811	0.225	0.00230	23.145	97.19	148.5	2.1	0.003708
8992-01C	24.366	0.216	0.00140	23.967	98.35	153.6	4.0	0.003708
8992-01D	25.943	-1.274	0.00589	24.066	92.85	154.2	5.6	0.003708
8992-01E	25.664	0.177	0.00418	24.433	95.20	156.5	6.7	0.003708
8992-01F	24.002	-0.359	0.00069	23.763	99.03	152.3	4.1	0.003708
8992-01G	24.228	0.028	0.02020	18.199	75.12	117.8	5.2	0.003708
8992-01H	21.532	-2.660	0.02820	12.885	59.95	84.2	6.9	0.003708
8992-01I	22.878	0.060	0.02923	14.156	61.88	92.3	5.8	0.003708
8992-02A	27.266	0.073	0.00683	25.235	92.55	161.4	1.1	0.003708
8992-02B	23.501	0.242	0.00198	22.932	97.56	147.2	1.2	0.003708
8992-02C	22.740	0.292	0.00213	22.128	97.29	142.3	3.2	0.003708
8992-02D	24.001	-0.460	0.00599	22.168	92.39	142.5	3.4	0.003708
8992-02E	24.882	0.000	0.01089	21.629	86.93	139.2	4.9	0.003708
8992-02F	22.896	0.609	#######	23.145	101.05	148.5	6.2	0.003708
8992-02G	19.891	-0.333	0.01051	16.722	84.09	108.5	3.8	0.003708
8992-02H	19.206	-0.154	0.02296	12.337	64.25	80.7	3.3	0.003708
8992-02I	19.205	-0.541	0.02665	11.204	58.36	73.4	4.8	0.003708
8992-02J	21.477	-3.312	0.03693	10.172	47.47	66.8	12.6	0.003708
Sample DQ70								
8985-01A	22.572	0.004	0.00196	21.985	97.41	140.1	0.5	0.003672
8985-01B	20.258	0.062	0.00013	20.224	99.83	129.2	2.0	0.003672
8985-01C	20.018	0.246	#######	20.775	103.76	132.6	2.9	0.003672
8985-01D	20.328	-0.448	#######	21.655	106.57	138.0	6.2	0.003672
8985-01E	20.943	0.949	0.00021	20.968	100.06	133.8	6.0	0.003672

8985-01F	21.445	0.208	0.00410	20.239	94.36	129.3	10.1	0.003672
8985-01G	18.414	0.094	0.00099	18.127	98.44	116.3	20.7	0.003672
8985-01H	18.300	0.115	0.00292	17.438	95.29	112.0	29.5	0.003672
8985-01I	30.925	-0.212	0.02760	22.664	73.30	144.2	25.6	0.003672
8985-01J	176.593	2.089	0.54877	12.931	7.31	83.7	34.0	0.003672
8985-02A	172.742	13.228	0.48451	29.370	16.85	184.8	16.3	0.003672
8985-02B	30.287	45.100	0.10302	3.085	9.87	20.3	19.3	0.003672
8985-02C	29.102	57.499	0.10468	2.357	7.78	15.5	16.0	0.003672
8985-02D	29.119	62.235	0.11622	-0.841	-2.76	-5.6	12.6	0.003672
8985-02E	28.462	115.937	0.21306	-28.538	-92.24	-199.7	28.6	0.003672
8985-02F	33.206	203.831	0.97686	-282.622	-731.25	NaN	-4703.8	0.003672
Sample DQ55								
8984-01A	20.262	0.022	0.00060	20.083	99.12	128.4	0.4	0.003672
8984-01B	20.504	0.023	0.00093	20.227	98.65	129.3	0.5	0.003672
8984-01C	20.334	0.018	0.00058	20.162	99.16	128.9	0.4	0.003672
8984-01D	20.161	0.012	0.00034	20.060	99.50	128.2	0.3	0.003672
8984-01E	20.339	0.018	0.00056	20.173	99.19	128.9	0.3	0.003672
8984-01F	20.513	-0.050	0.00071	20.295	98.95	129.7	0.4	0.003672
8984-01G	20.826	0.067	0.00141	20.411	98.01	130.4	1.4	0.003672
8984-01H	20.577	-0.038	0.00137	20.163	97.99	128.9	0.6	0.003672
8984-01I	19.996	0.413	0.00217	19.386	96.92	124.1	2.6	0.003672
8984-01J	37.251	4.617	0.00396	36.541	97.78	227.1	62.3	0.003672
8984-02A	20.231	0.064	0.00118	19.884	98.28	127.1	0.6	0.003672
8984-02B	20.152	0.039	#######	20.198	100.23	129.1	0.4	0.003672
8984-02C	20.071	-0.022	0.00020	20.009	99.70	127.9	0.4	0.003672
8984-02D	20.216	0.018	0.00017	20.167	99.76	128.9	0.3	0.003672

8984-02E	20.305	0.004	0.00045	20.169	99.34	128.9	0.3	0.003672
8984-02F	20.370	0.021	0.00092	20.096	98.66	128.4	0.4	0.003672
8984-02G	20.671	-0.140	0.00111	20.326	98.34	129.9	1.0	0.003672
8984-02H	20.672	-0.018	0.00169	20.166	97.56	128.9	0.4	0.003672
8984-02I	20.894	-0.197	0.00350	19.831	94.93	126.8	2.0	0.003672
8984-02J	24.805	2.137	0.02449	17.682	71.18	113.5	17.0	0.003672
Sample DQ123								
8987-01A	21.025	0.011	0.00060	20.847	99.15	133.1	0.3	0.003672
8987-01B	20.220	0.008	0.00098	19.926	98.55	127.4	0.4	0.003672
8987-01C	20.412	0.010	0.00163	19.925	97.62	127.4	0.4	0.003672
8987-01D	20.312	0.007	0.00157	19.844	97.70	126.9	0.3	0.003672
8987-01E	19.939	0.025	0.00055	19.775	99.18	126.5	0.3	0.003672
8987-01F	20.027	-0.051	0.00020	19.961	99.68	127.6	0.3	0.003672
8987-01G	20.197	0.014	0.00085	19.944	98.75	127.5	0.4	0.003672
8987-01H	20.361	-0.025	0.00122	19.993	98.20	127.8	0.6	0.003672
8987-01I	20.463	-0.039	0.00190	19.891	97.21	127.2	0.5	0.003672
8987-01J	20.566	-0.098	0.00175	20.032	97.42	128.1	0.6	0.003672
8987-01K	47.100	-5.708	0.05885	28.972	61.76	182.4	52.6	0.003672
8987-02A	20.718	-0.007	0.00019	20.661	99.73	131.9	0.2	0.003672
8987-02B	20.143	-0.017	0.00033	20.041	99.50	128.1	0.3	0.003672
8987-02C	20.030	-0.022	0.00004	20.016	99.94	128.0	0.4	0.003672
8987-02D	20.022	-0.004	0.00002	20.015	99.97	127.9	0.4	0.003672
8987-02E	20.054	0.008	0.00026	19.976	99.62	127.7	0.3	0.003672
8987-02F	20.185	-0.024	0.00036	20.073	99.45	128.3	0.3	0.003672
8987-02G	20.363	-0.047	0.00036	20.249	99.45	129.4	0.3	0.003672
8987-02H	20.491	-0.008	0.00015	20.446	99.78	130.6	0.4	0.003672

8987-02I	20.929	0.083	0.00039	20.821	99.48	132.9	1.2	0.003672
8987-02J	20.718	-0.071	0.00041	20.586	99.38	131.5	0.6	0.003672
8987-02K	30.837	-6.735	0.00087	29.921	97.48	188.1	25.0	0.003672

Note: The terms $^{40}Ar^*$ and $^{39}Ar_K$ denote radiogenic ^{40}Ar and nucleogenic ^{39}Ar, respectively.